Università degli Studi di Ferrara

DOCTORAL COURSE IN
"PHYSICS"

CYCLE XXXVIII

COORDINATOR Prof. Paolo Lenisa

Development and Application of a Generalized Model for Systematic Drift Error Correction in Applied Microgravity

Scientific/Disciplinary Sector (SDS) FIS / 06

Candidate
Dott. Petrone Dario

Supervisor
Prof. Mantovani Fabio

Year 2022/2025

Contents

Introduction

Microgravity is an indirect geophysical method that uses high-precision gravity measurements to infer near-surface density variations at the local scale [1], [2], [3]. Its ability to resolve anomalies of a few microgals (1 μGal = 10^{-8} m s^{-2}), this resolution supports applied uses such as geological/hydrogeological monitoring. It is also used for cavity and sinkhole detection and for buried infrastructure mapping [4], [5], [6]. Advances in instrumentation, acquisition practice, and processing workflows have strengthened the role of microgravity in applied and industrial contexts, where dense sampling and rapid turnaround are primary operational constraints [7], [8].

Industrial microgravity is used here to indicate operational surveys carried out by private companies (engineering, environmental, and infrastructure services), whose requirements are not directly comparable with research-oriented gravimetry. Field campaigns often require many stations in short time windows, sometimes on very dense grids (up to hundreds of stations per day). This pushes workflows toward streamlined and repeatable procedures integrated in production. Measurements are typically performed in challenging settings dominated by anthropogenic noise and operational disturbances (roads, highways, construction sites, and built infrastructure), together with vibrations, thermal gradients, and mechanical perturbations that can degrade data quality and modulate instrument response. Under these conditions, even small systematic biases may compromise the interpretation of subtle microgravity anomalies, making robust and standardizable correction procedures essential.

Industrial surveys commonly employ portable relative gravimeters with high mechanical sensitivity. Among them, the Scintrex CG-5 Autograv is one of the most widely used instruments in engineering and environmental applications. The CG-5 combines a quartz spring sensor with electronic feedback to maintain force balance, providing relative gravity differences with nominal accuracy better than 5 μGal under ideal conditions [9], [10]. The instrument is compact and fast to deploy, and acquisition is automated. This makes it practical for short-baseline, high-resolution surveys in urban, coastal and mountainous settings.

Like all spring-based gravimeters, the CG-5 is affected by instrumental drift, i.e., a slow temporal change in measured gravity that is unrelated to true variations of the gravitational field [7], [11]. Drift rates of tens to hundreds of microgals over days to weeks have been reported [8], [9], [12] and may exceed the amplitude of target anomalies; therefore, drift must be estimated and removed from time series [13], [14].

Conventional drift corrections based on linear trends or low-order polynomials inferred from repeated base-station readings at the beginning and end of survey lines or days [4], [13] implicitly assume a monotonic and stationary behavior. However, CG-5 drift may include slow, quasi-periodic fluctuations superimposed on the long-term component [8], [12], [15]. In such cases, linear correction can leave deterministic residuals that propagate into the final gravity field and may mimic signals of interest [5], [8]. This limitation is particularly critical for industrial microgravity, where dense station spacing and environmental disturbances reduce tolerance to systematic errors.

Current drift-correction methods for the CG-5 lack a standardized and physically interpretable protocol capable of describing and correcting the non-linear, time-dependent drift of the CG-5 under different operational conditions. Previous studies have addressed specific aspects of CG-5 performance (e.g., tilt sensitivity [16], calibration stability [17], and scale-factor variability [12]), but a comprehensive, field-validated model that consistently represents both deterministic and stochastic components of drift over a broad temporal range is still missing.

The objective is to define and validate a harmonic correction protocol for the systematic temporal bias in CG-5 data that is compatible with industrial microgravity workflows. The approach is motivated by base-station time series that consistently exhibit structured temporal variability, indicating the presence of coherent drift components acting on different timescales.

The slow drift component is first corrected using up to three low-frequency harmonic terms, with periods constrained between ten and one hundred days, together with a constant offset. This stage targets the long-term evolution of the gravimeter response and absorbs persistent low-frequency signals that may remain after standard tidal corrections. To account for shorter-period systematic effects that are not adequately represented at this stage, an additional correction is applied when necessary, modelling the remaining temporal bias with up to two higher-frequency harmonic terms, with search periods constrained between twelve and forty-eight hours. This second stage captures sub-daily and near-diurnal oscillations commonly observed in CG-5 base-station records.

The analysis is intentionally limited to the temporal behaviour of the base-station series and therefore excludes spatial reductions (free-air, Bouguer, and terrain corrections).

The protocol is tested on an extensive dataset of repeated surveys acquired between 2021 and 2025 across heterogeneous geological and environmental settings.

For comparison under more controlled conditions, a short time series acquired at the San Giovanni calibration site is also analysed as a reference dataset with minimized environmental forcing (Chapter 3).

This thesis investigates the extent to which the systematic temporal variability observed in CG-5 base-station records can be described by a compact harmonic representation combined with a constant offset. In particular, the work evaluates whether a multi-harmonic correction is capable of reducing post-correction residuals to within the instrumental precision of the CG-5 across heterogeneous operational conditions, and whether the inferred periodic components are reproducible across independent surveys and acquisition campaigns.

The resulting outcome is a validated and transferable correction workflow for CG-5 base-station data in industrial microgravity applications, providing residual stability compatible with the precision requirements of applied investigations.

1 Systematic temporal bias in CG-5 applied microgravity

Operational microgravity requires temporal stability at fixed benchmarks because target anomalies are commonly in the tens-to-hundreds of μGal [5], [6]. However, CG-5 records show systematic low-frequency variability that can dominate the error budget over days to weeks [7]. This chapter summarizes how systematic temporal bias appears in base-station records, reviews the main instrumental and operational drivers, and outlines why purely empirical corrections are often insufficient.

1.1 Evidence from repeated-base occupations

High-precision microgravity depends on temporal consistency at invariant reference points, yet fixed-station CG-5 time series are not purely stochastic. Even after standard corrections, low-frequency drift and structured residuals commonly persist and can reach amplitudes comparable to, or larger than, expected survey anomalies [7]. In routine field practice, this behaviour is sampled through repeated base-station reoccupations: readings change systematically with time and often show reproducible curvature. Step-like discontinuities can also occur, for example following memory handling or operational resets [8], [12]. As a consequence, short-term reading precision alone is not a reliable proxy for data quality; time-dependent bias must be explicitly addressed to avoid imprinting temporal structure into the mapped spatial anomaly field [13], [14]. These observations indicate that the observed temporal variability cannot be attributed to random noise alone, but reflects systematic contributions whose origin must be examined in terms of both instrument behaviour and survey practice.

1.2 Sources of systematic temporal bias: instrumental and operational

Low-frequency variability reflects the superposition of instrumental and operational contributions that overlap in the same spectral band. Instrument-internal processes, including thermal equilibration and quartz-spring relaxation, can generate smooth temporal trends over hours to weeks.[7], [9]. The CG-5 is also sensitive to tilt, and residual tilts can introduce measurable offsets consistent with reported instrument susceptibility [16]. In addition, deterministic corrections may leave structured residuals: Although the CG-5 applies an internal tidal correction (Longman-type formulation [18]), residual tidal components may remain in the corrected series. Instrument metrology can further contribute, as reading-dependent scale factors and apparent calibration shifts reported in long records suggest partial coupling between drift and scale [12], [17], [19].

In applied surveys, these effects are compounded by operational forcing (transport, vibrations, temperature gradients, and access constraints), yielding composite temporal behaviour that is not well represented by a single monotonic trend.

1.3 Instrument response characteristics relevant to temporal stability

The Scintrex CG-5 is a relative gravimeter based on a quartz spring sensing element operating within a closed-loop feedback system. Variations in the local gravity field produce a displacement of the spring–mass system, which is continuously counteracted by an electrostatic feedback force to restore the sensing element to its nominal position. The gravity signal is thus inferred from the feedback required to maintain equilibrium, rather than from a direct static deflection. As a consequence, CG-5 measurements represent the output of a dynamic physical system rather than instantaneous samples of the gravity field.

The instrument response is inherently continuous in time and affected by internal relaxation processes. The operating manual explicitly notes that the spring system requires thermal and mechanical stabilization after transport and handling, and that gradual changes in the instrument response can occur even under constant external gravity conditions. These effects are routinely addressed in field practice through warm-up periods and repeated base-station occupations, indicating that the instrument does not behave as an ideal time-invariant sensor.

In addition to the mechanical sensing element, the CG-5 applies internal corrections for tilt, temperature, and tides using embedded sensors and deterministic models. While these corrections reduce known sources of variability, they do not eliminate all temporal structure in the recorded signal. Residual components may persist due to incomplete modelling, instrument sensitivity to small uncorrected perturbations, or coupling between internal correction terms and the feedback-controlled spring system. The combined action of elastic relaxation, feedback control, and deterministic corrections therefore yields a temporal response that is smooth but not purely monotonic.

This behaviour has direct implications for drift modelling. A spring-based gravimeter operating in closed loop is expected to exhibit time-dependent responses that evolve gradually and may contain structured components rather than a single linear trend. When the response is slow and internally structured, representing the deterministic component of the temporal bias with a compact set of harmonic terms becomes a physically motivated choice rather than a purely empirical adjustment. This perspective directly informs the drift-modelling strategy adopted in the following sections.

1.4 Limits of empirical drift correction

Despite these physical considerations, most applied microgravity workflows still rely on empirical drift-removal strategies. In applied workflows, drift is commonly removed as an empirical trend constrained by base-station reoccupations, typically linear per day or per campaign[4], [13]. Polynomial detrending is sometimes used to capture curvature over multi-day windows [7], and higher-degree polynomials have been explored with degree selection based primarily on residual statistics rather than physical arguments [15]. Many CG-5 studies adopt linear drift removal as a pragmatic step when the analysis focuses on other error sources, implicitly assuming local linearity within restricted time windows [8], [12]. Some processing toolchains similarly implement detrending as a flexible, data-driven correction stage [20]. Although these approaches can reduce gross drift, they suffer from two structural limitations: (i) fitted parameters depend on segmentation choices and operator decisions, and (ii) repeatable low-frequency structure (e.g., quasi-periodic components or step-like events) may persist in the residuals and propagate into the spatial interpretation, especially as campaign duration increases or operational conditions vary [8], [12], [15].

1.5 A harmonic correction protocol for systematic temporal bias

The central methodological gap is therefore not the existence of drift, but the lack of a transferable field protocol that isolates the deterministic component with a compact parameterization, remains stable across heterogeneous sites, and is compatible with industrial constraints (dense grids, limited time, variable access, frequent transport). The synthesis above indicates that:

- structured temporal variability is common in fixed-station records [7], [8];
- multiple instrumental and operational contributors overlap in the same low-frequency band [9], [12], [16], [17];
- empirical trends (linear/polynomial) can be insufficient when deterministic structure persists [8], [12], [15].

Together, these considerations motivate modelling the deterministic component of the systematic temporal bias using a limited set of harmonic terms plus operational offsets, providing a compact, physically grounded, and transferable correction framework suitable for applied microgravity surveys.

2 Datasets: laboratory benchmark and field surveys

A set of microgravity surveys acquired in different geological, environmental and operational contexts is presented as the experimental basis for the analysis of systematic temporal bias developed in this thesis. Although each dataset originates from an applied or industrial investigation—such as cavity detection, subsurface stability assessment or sinkhole hazard evaluation—the sites are not treated as independent geological case studies. Instead, they are reinterpreted as repeated gravimetric measurements performed at fixed reference points over time under realistic field conditions.

All gravity time series presented in this chapter refer to data already corrected for tidal effects, and where memory resets occurred, step-like offsets associated with cumulative memory effects have been removed. These preprocessing steps ensure temporal continuity of the base-station records; the methodological details of tide correction and memory-jump handling are described in chapter 3.1.

In the absence of true temporal mass changes at the base station, gravity values are expected to remain constant within measurement uncertainty. The systematic deviations observed across the datasets therefore reflect the combined influence of instrumental drift, operational events, and site-dependent exogenous noise. The deliberate inclusion of sites characterised by contrasting lithologies, topography, and levels of anthropogenic interference allows the persistence and variability of these effects to be assessed beyond idealised conditions.

For each site, the presentation is intentionally compact and organised around three elements: a concise geological and environmental framework limited to factors relevant to gravity stability, the operational objectives and survey configuration with emphasis on base-station management, and the analysis of base-station time series. Unless otherwise stated, gravity data were collected with a Scintrex CG-5 Autograv at 6 Hz using 60 s integrations and processed with standard on-board corrections. This consistent structure facilitates comparison across sites and provides the observational foundation for the harmonic correction approach introduced in chapter 3, aimed at mitigating systematic temporal bias in applied CG-5 microgravimetry.

2.1 Brica di Sillano (Tuscany, Italy)

2.1.1 Geological and environmental setting

The Brica di Sillano site is located within the Tuscan Domain of the Northern Apennines, where fractured carbonate units of the *Falda Toscana* are tectonically juxtaposed with low-permeability argillaceous formations. The investigated sector is characterised by strong lateral and vertical density contrasts associated with massive platform carbonates, cherty-carbonate units and interbedded clay-rich formations, locally covered by heterogeneous colluvial and debris deposits [21], [22]. This litho-structural configuration favours the development of shallow voids, preferential drainage paths and localized instability, which motivated the application of high-resolution industrial microgravity for subsurface screening along a planned pipeline corridor.

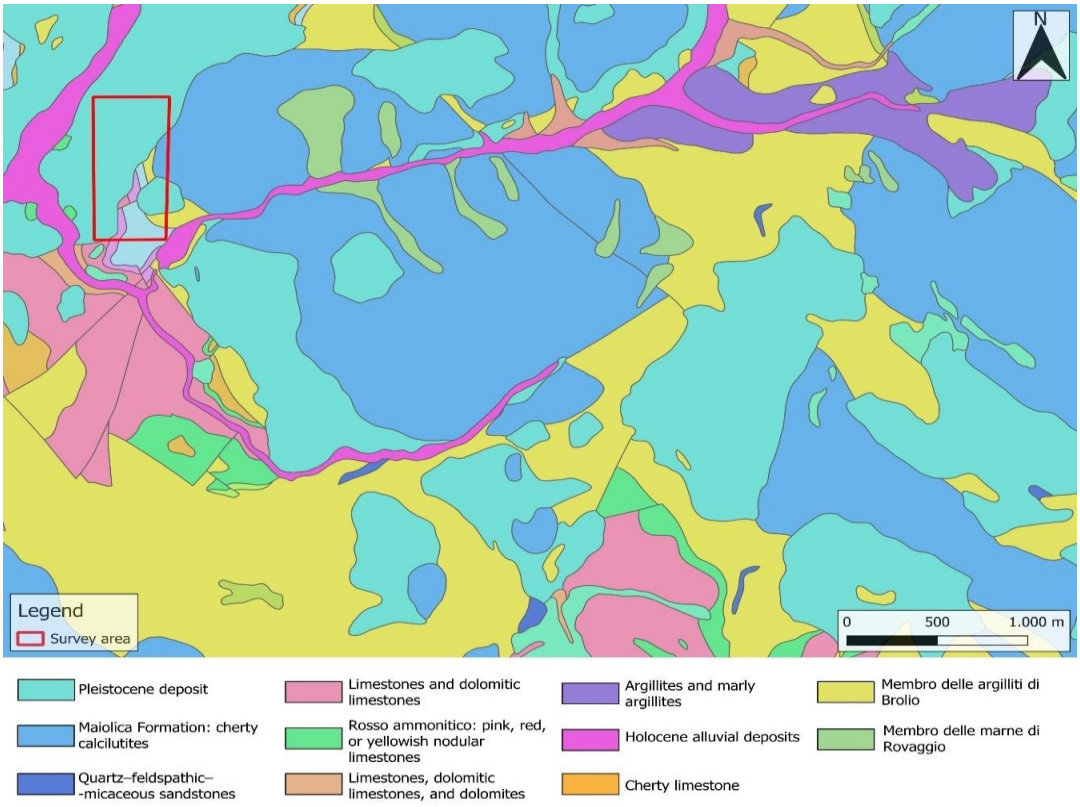

Figure 1. Geological framework of the Brica di Sillano survey area derived from the CARG geological map (WMS). The survey window (red rectangle) overlies Pleistocene–Holocene deposits, fractured carbonate and cherty-carbonate units, and interbedded argillaceous and sandstone formations. Local units discussed in the text are grouped into three main classes: platform and pelagic carbonates (Calcare Massiccio, Calcari ad Angulati, Rosso Ammonitico, Maiolica), argillaceous formations (Scisti Policromi, marly argillites), and quartz–feldspathic–micaceous sandstones (Macigno). Scale bar in metres; north arrow at top right. Data source: CARG — Carta Geologica d'Italia (WMS).

From a hydrogeological perspective, the area belongs to a highly permeable fractured- and karst-carbonate aquifer system subject to rapid recharge, sustained by high mean annual precipitation [23]. The coexistence of fast infiltration in fractured carbonates and low-permeability layers produces transient variations in water content at shallow depth, potentially inducing short-term mass redistribution at the scale of hours to days. Although these processes may generate low-amplitude exogenous gravity signals, their expected magnitude is small compared to the long-period systematic trends observed in the base-station records.

2.1.2 Objectives and operational framework

The Brica campaign targeted shallow voids along a gas-pipeline corridor. For this thesis, the dataset provides a stringent test of drift correction under demanding mountain conditions, with daily gravimeter transport between 500–1000 m a.s.l. introducing thermal and mechanical perturbations.

The survey was conducted along four linear transects on an accessible slope bench, with ~1 m station spacing (87–107 stations per line), aligned with the pipeline corridor (Figure 2). A base station on stable ground was reoccupied twice daily to segment acquisition into consistent intervals. Data were collected between 16 and 31 March 2021.

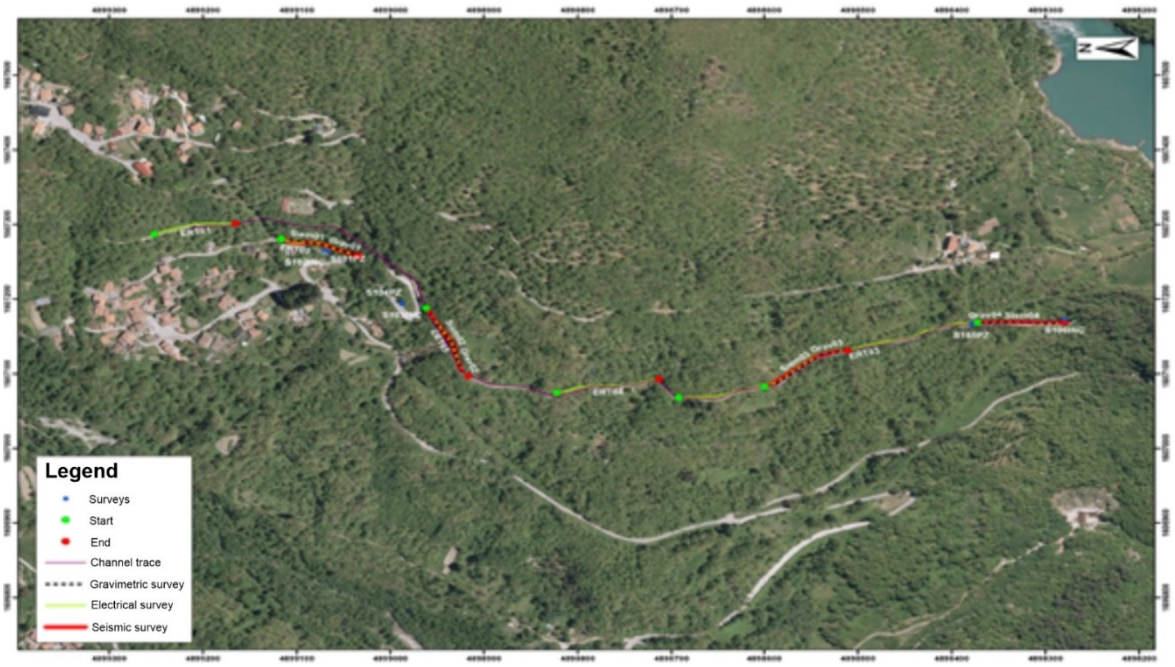

Figure 2. Orthoimage showing the distribution of microgravity stations along the investigated corridor, together with boreholes, electrical resistivity profiles and seismic profile.

Due to dense vegetation and canopy shadow, GNSS RTK corrections were unreliable; station positions were therefore measured with a Leica MS50 robotic total station, which ensured centimetric accuracy along the narrow bench [24]. The main operational parameters and survey characteristics are summarised in Table 1.

Table 1. Field acquisition summary — Brica di Sillano (Tuscany, Italy).

Item	Details
Site	Brica di Sillano, mountain slope sector (gas pipeline corridor), Tuscany, Italy
Acquisition period	March 2021
Industrial microgravity target	Shallow voids / density contrasts along the trench axis of a buried pipeline
Operational objective	Exclude cavities and unstable zones along the pipeline route
Dominant lithology	Slope debris/colluvium over flysch formations of the Northern Apennines (local flysch units)
Topographic instrument	Leica MS50 robotic total station
Gravity instrument	Scintrex CG-5 Autograv
Total number stations	404
Station spacing	1 m along four transects
Acquisition parameters	60 s – 6 Hz

2.1.3 Analysis of raw base-station data

The base-station record spans approximately sixteen days and is segmented by semidiurnal reoccupations (Figure 3). The sequence documents smooth, nearly monotonic trends within each acquisition segment, with gaps marking the reoccupation cadence used to maintain temporal control. Late in the campaign a discrete level shift appears between two consecutive segments, producing a step of the order of 10 mGal; field operations indicate that this discontinuity corresponds to a memory-cancellation/reset event. Earlier segments do not display step changes at the scale of Figure 3, and the overall series therefore preserves both the intra-segment continuity and the operational discontinuity associated with the reset.

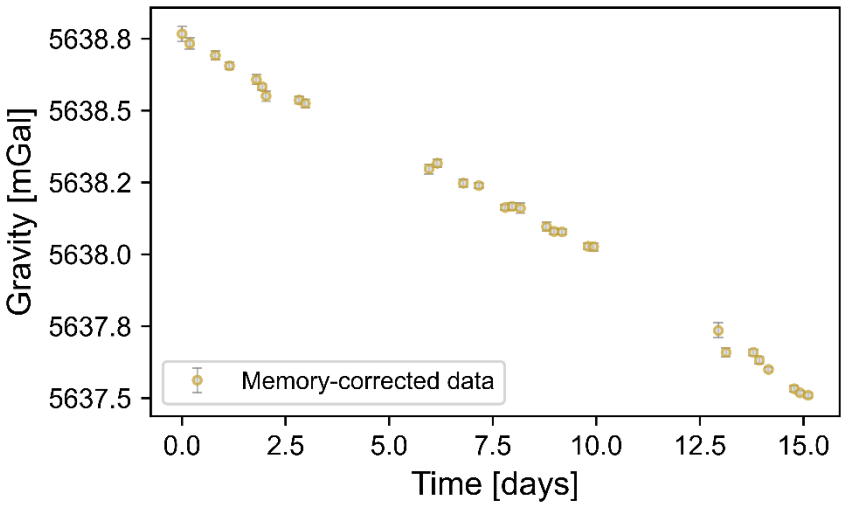

Figure 3. Gravity time series for the Brica di Sillano base station. Unprocessed gravity measurements showing a distinct step discontinuity associated with the instrument's memory reset event. This offset represents a characteristic artifact of the CG-5 Autograv.

Measurement stability per reading is shown by the internal SD computed during each 60-s acquisition. The SD dot-plot (Figure 4 indicates a predominantly low-to-moderate noise regime, with SD values clustered around the median of 13 µGal (Table 2). Most readings fall in a compact band (roughly in the low-teens of µGal), consistent with generally stable conditions during the base reoccupations. A sparse upper tail reaches ~27 µGal, which points to episodic transient disturbances affecting a limited number of readings.

The record is adequate for systematic bias analysis. The few higher-SD readings mark intervals with increased external noise. One memory reset was detected during acquisition.

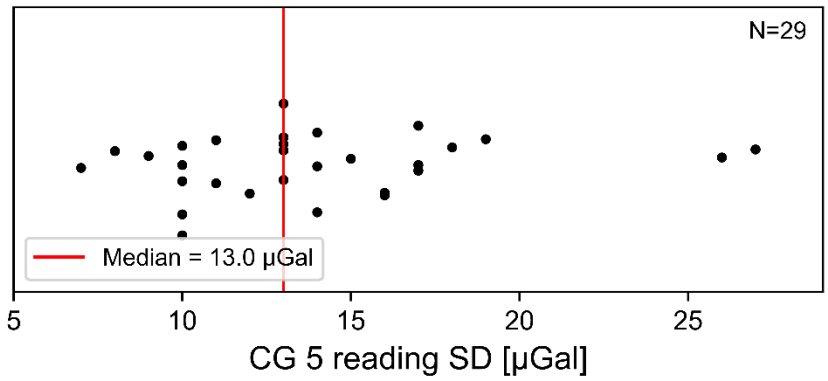

Figure 4. Brica di Sillano—CG-5 internal SD per reading (60 s integration; 6 Hz sampling). Points show per-reading SD; red line marks the median; N indicates the number of readings.

Table 2. Statistical parameters describing the quality and stability of the base-station dataset acquired at Brica

Parameter	Value / Observation
Number of readings	29
Mean SD (µGal)	14
Median SD (µGal)	13
Standard deviation SD (µGal)	5
Minimum SD (µGal)	7
Maximum SD (µGal)	27
Memory resets detected	1

2.2 Pigneto (Lazio, Italy)

2.2.1 Geological and environmental setting

The Pigneto district is located in eastern Rome, within the Prenestino–Labicano sector, at the transition between the volcanic plateaus of the Roman Campagna and the Tiber alluvial plain. The subsurface is characterised by a heterogeneous volcanic succession emplaced during Middle–Upper Pleistocene activity of the Roman Comagmatic Province, resting on Pliocene marine clayey–sandy deposits of the Monte Vaticano Formation. Within the survey window (Figure 5), the dominant lithologies consist of lithoid and stratified tuffs, tuffites and earthy tuffs, locally interbedded with anthropogenic fills and minor alluvial deposits, producing strong lateral variability in bulk density and mechanical properties at shallow depth. A distinctive feature of the area is the widespread presence of ancient underground quarries excavated in volcanic tuffs and subsequently reused as cisterns, storage chambers and catacombs, many of which are incompletely mapped and typically located at depths of 5–15 m.[25], [26]. The superposition of porous volcanic units, anthropogenic cavities, unconsolidated backfill and urban loads defines a subsurface environment prone to localized instability and sinkhole formation, as documented by official hazard maps that classify the Pigneto area among the most critical sectors of eastern Rome (Figure 6).

From a hydrogeological perspective, the alternation of permeable volcanic deposits and less-permeable clay-rich horizons produces a shallow unconfined aquifer overlying a deeper regional groundwater system [27]. In the urban setting, leakage from buried utilities and discontinuous aquitards induce time-dependent variations in shallow water content, which may generate low-amplitude exogenous gravity signals on short timescales. Consequently, the Pigneto site provides a representative urban test case in which instrument-related temporal variability and operational effects dominate the evolution of the gravity record, offering a demanding dataset for evaluating temporal-bias correction in a high-interference setting.

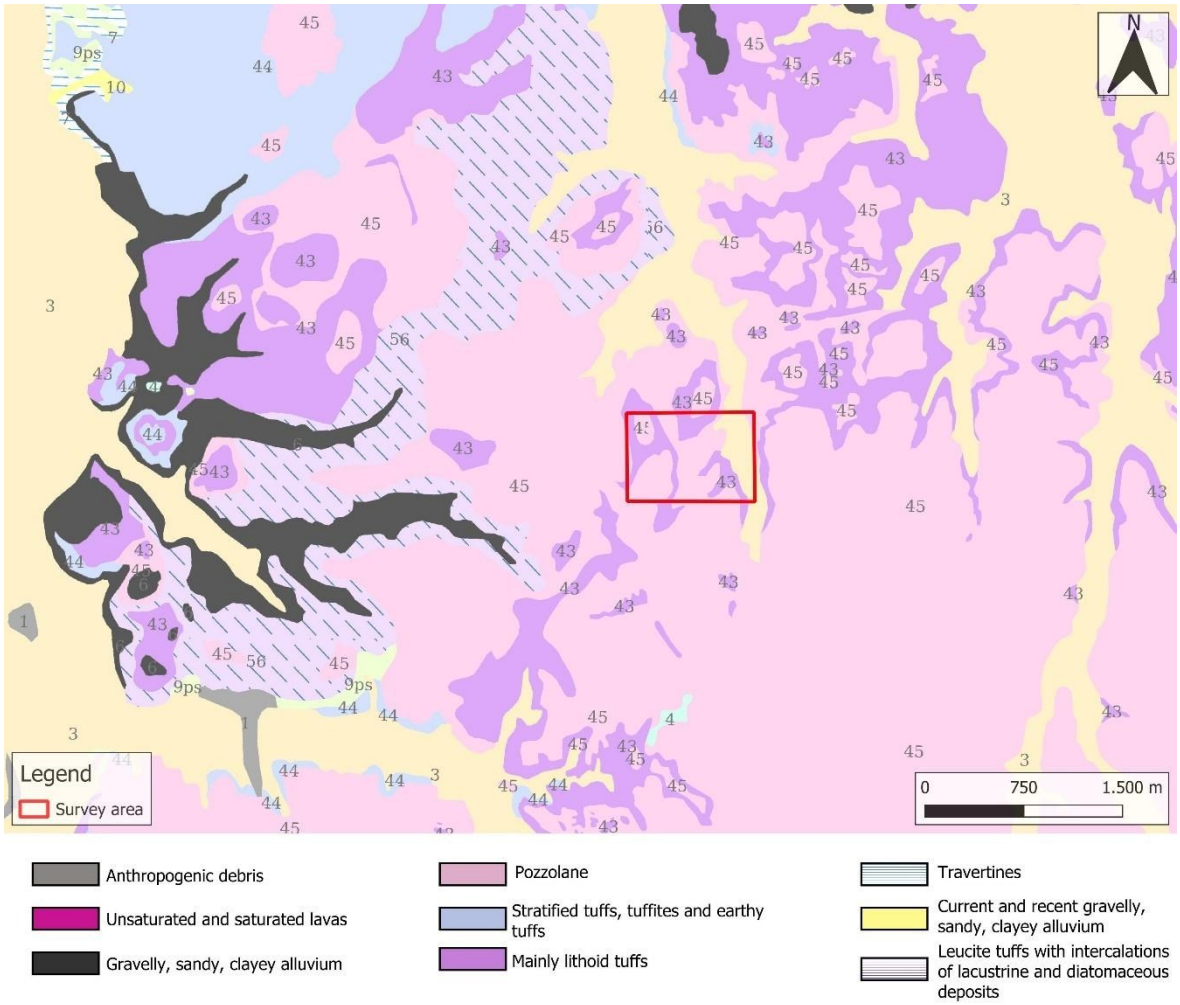

Figure 5. Geological framework of the Pigneto survey area (Rome). The survey window (red rectangle) overlies units from the CARG geological map (WMS). Legend classes present within the window: pozzolane; mainly lithoid tuffs (code 45); stratified tuffs, tuffites and earthy tuffs (code 43); current and recent gravelly, sandy, clayey alluvium; anthropogenic debris. Numbers indicate formation codes as in the CARG sheet. Scale bar in metres; north arrow at top right. Data source: Regione Lazio Geoportal, WMS "CARG – Carta Geologica d'Italia" (accessed 2025).

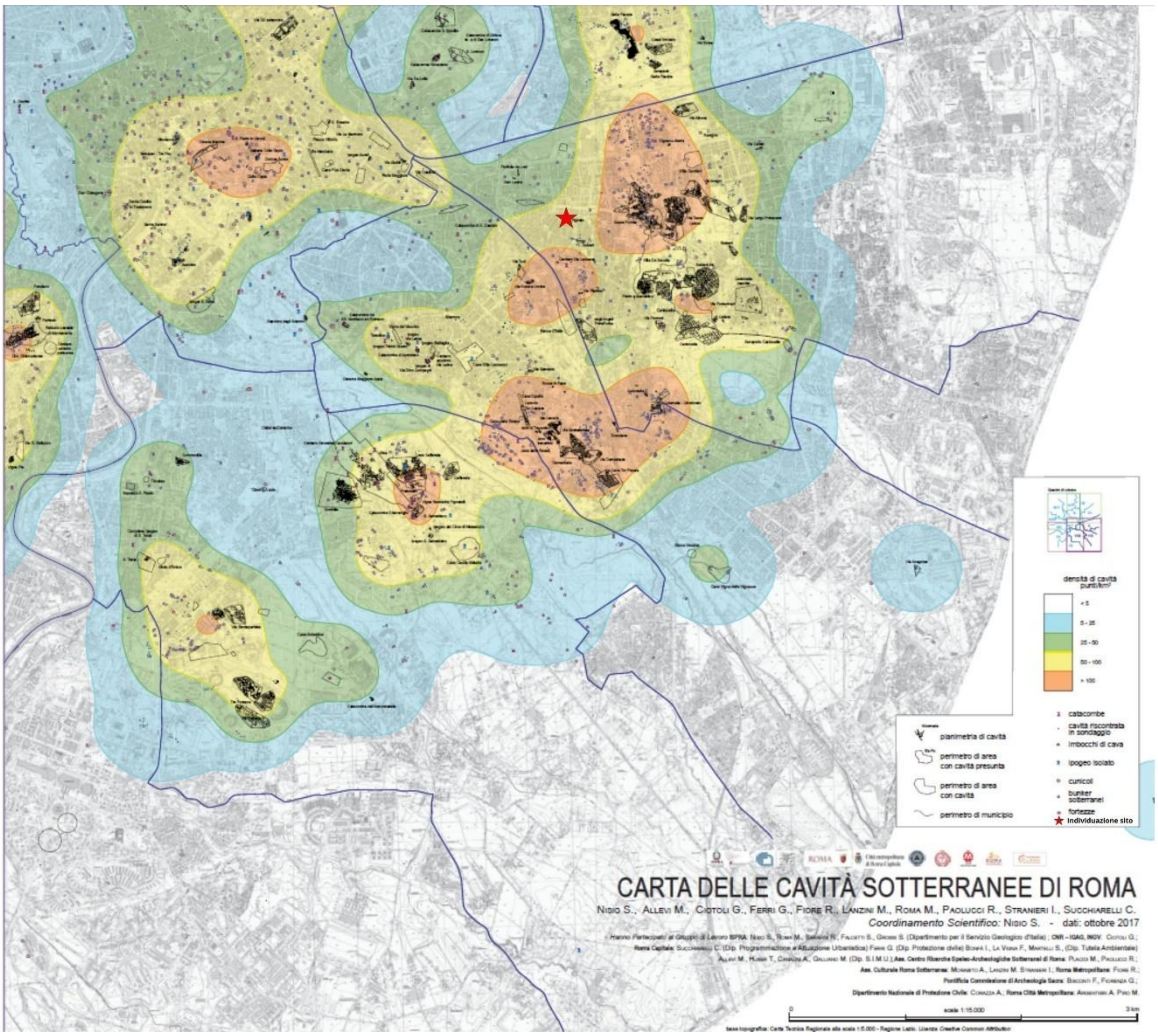

Figure 6. Sinkhole hazard map of the southeastern sector of Rome. The map illustrates the distribution of subsurface cavities and sinkhole-prone areas across the urban territory. The yellow-shaded zones indicate medium sinkhole susceptibility, while the red star marks the Pigneto district, located within one of the most critical areas for underground instability in the southeastern quadrant of the city [28].

2.2.2 Objectives and operational framework

The industrial objective of the Pigneto survey was the detection and delineation of shallow underground cavities and low-density zones in a densely urbanised setting, with the aim of assessing sinkhole susceptibility and supporting risk mitigation strategies for surface infrastructure. The dataset is reanalysed as a controlled urban experiment with substantial anthropogenic interference, providing a demanding test case for assessing and correcting instrument-related drift within the broader systematic temporal bias of the CG-5 record.

Figure 7. Survey layout of the Pigneto district, Rome. Aerial view showing the microgravity measurement network and base station locations along the urban streets of the Pigneto area. The survey design follows the main road intersections to maximize spatial coverage and detect potential subsurface anomalies related to sinkhole susceptibility beneath the built environment.

Gravity measurements were acquired over a compact grid deployed within a constrained urban area, where station spacing and layout were dictated by surface accessibility, traffic conditions and existing infrastructure. Base reoccupation followed a 3–4 times/day schedule to maintain drift control. Positioning relied on local topographic control and GNSS-based referencing where satellite visibility allowed, with elevations referred to orthometric heights via the Italian quasi-geoid models [29]. The main acquisition parameters and operational constraints are summarised in Table 3.

Table 3. Field acquisition summary — Pigneto (Rome, Italy).

Item	Details
Site	Pigneto district, eastern Rome (Prenestino–Labicano sector), Italy
Acquisition period	March 2022
Industrial microgravity target	Anthropogenic cavities/low-density bodies in urban tuffs and shallow cover
Operational objective	Subsurface stability screening in a densely urbanized block affected by historical quarrying
Dominant lithology	Stratified volcanic tuffs over Monte Vaticano clayey bedrock
Topographic instrument	Leica MS50 robotic total station
Gravity instrument	Scintrex CG-5 Autograv
Total number stations	400
Station spacing	2 m (regular grid)
Acquisition parameters	60 s – 6 Hz

2.2.3 Analysis of raw base-station data

The base-station series spans approximately six days and documents the full sequence of daily reoccupations (Figure 8). Within this short campaign, the gravity readings show distinct acquisition segments separated by reoccupation gaps, as expected under constrained urban scheduling. A step offset of about 300 mGal occurs between the initial and subsequent segments, clearly attributable to a memory reset operation, after which the signal resumes a stable trend. Within individual segments, readings display smooth and internally consistent behavior without evidence of abrupt instability.

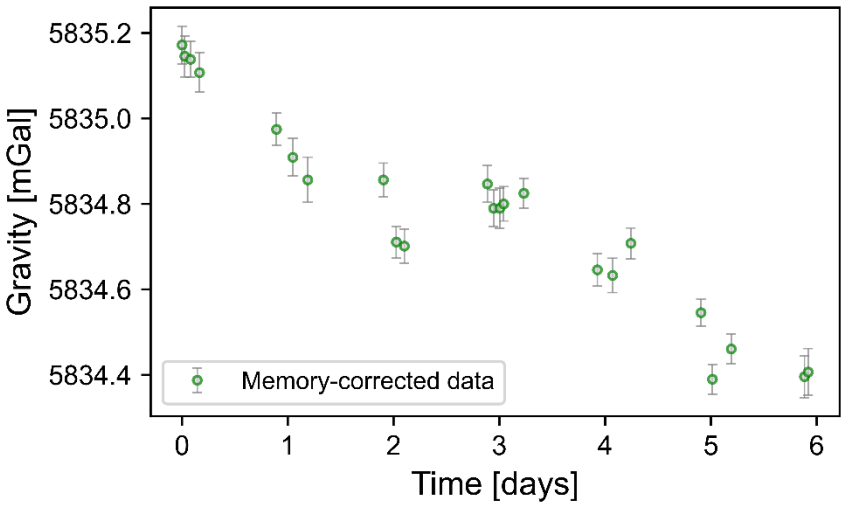

Figure 8. Gravity time series acquired at the Pigneto site. the dataset reveals two discontinuities corresponding to consecutive memory reset operations of the cg-5 gravimeter. These step-like jumps highlight the impact of memory resets operations on the apparent long-term trend of the raw gravity signal.

For the Pigneto base-station dataset, the within-reading variability reported by the instrument (internal SD) summarises short-term noise conditions. In contrast to the lower-noise sites, the SD dot-plot (Figure 9), shows values systematically shifted toward higher scatter, with a central tendency at 40 µGal and a broad distribution extending up to 55 µGal. The corresponding statistics (Table 4) confirm this elevated noise level: mean 42 µGal, standard deviation 6 µGal, and range 31–55 µGal over n = 23 readings. This pattern is consistent with sustained cultural vibration typical of an urban setting (e.g., traffic-induced microvibrations and local anthropogenic activity), which increases the short-period variability of the stacked samples within each reading.

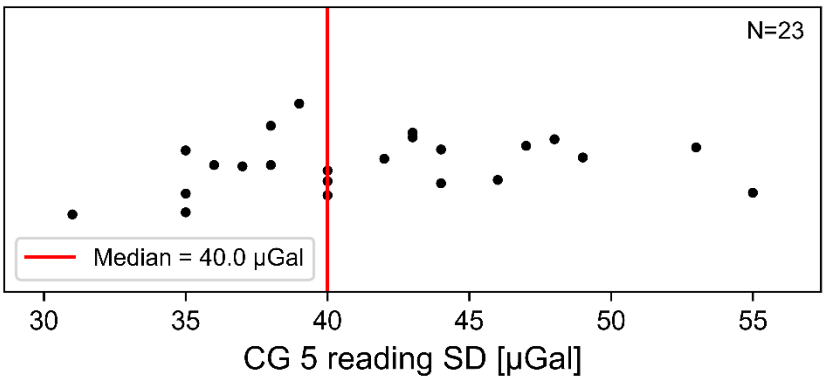

Figure 9. Pigneto—CG-5 internal SD per reading (60 s integration; 6 Hz sampling). Points show per-reading SD; red line marks the median; N indicates the number of readings.

Table 4. Statistical parameters describing the quality and stability of the base-station dataset acquired at Pigneto

Parameter	Value / Observation
Number of readings	23
Mean SD (µGal)	42
Median SD (µGal)	40
Standard deviation SD (µGal)	6
Minimum SD (µGal)	31
Maximum SD (µGal)	55
Memory resets detected	2

2.3 Bagni di Tivoli (Lazio, Italy)

2.3.1 Geological and environmental setting

The Bagni di Tivoli survey area is located east of Rome, on the travertine plateau of the Acque Albule basin along the Aniene valley. The near-surface geology is dominated by porous and heterogeneous hydrothermal travertines (TBTC unit), locally overlying more compact lithoid travertines and surrounded by volcanic tuffs and recent alluvial deposits (Figure 10) [25]. Fault-controlled hydrothermal circulation in the area enhances permeability and promotes selective dissolution within the travertine body. From the perspective of this study, the relevance of the site lies in the combination of high porosity, active groundwater circulation, elevated humidity, and persistent anthropogenic disturbance, all of which may influence the thermal and mechanical stability of the gravimeter without inducing true temporal mass changes at the base-station location.

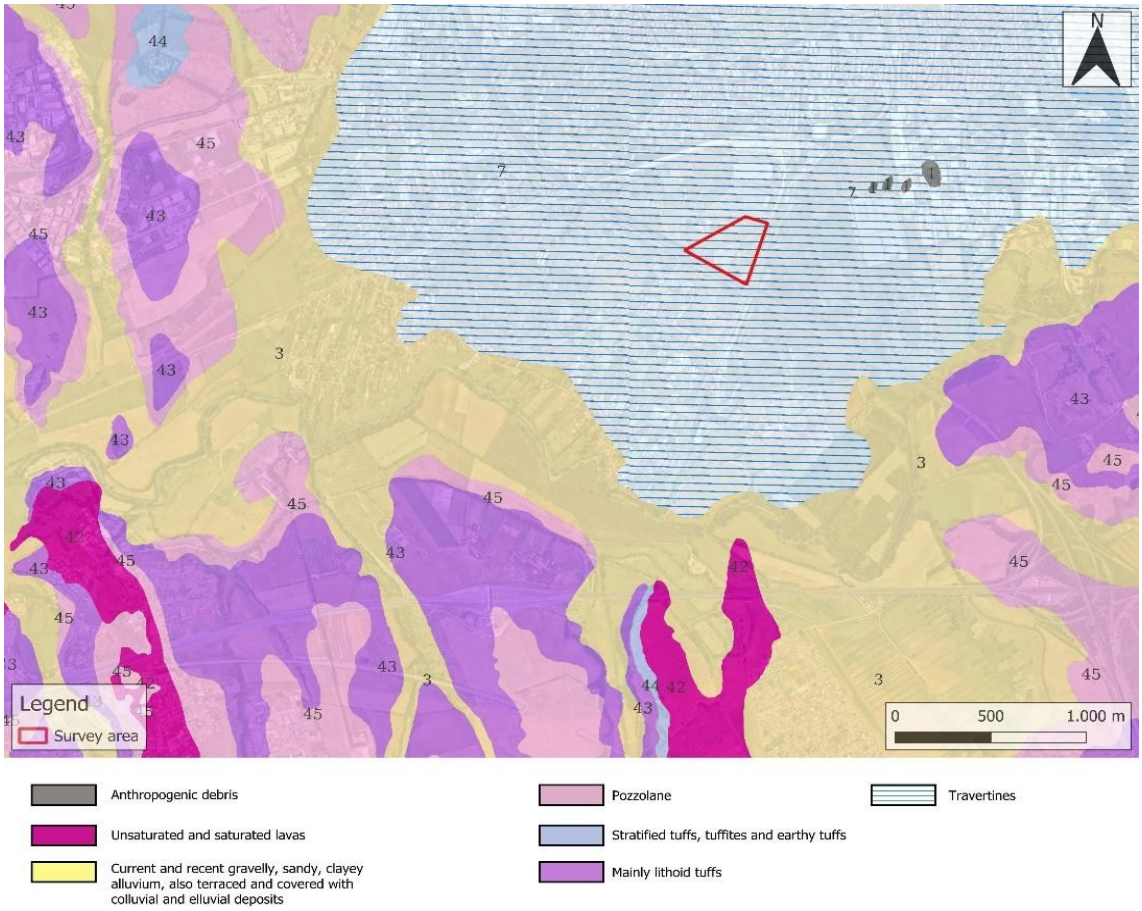

Figure 10. Geological framework of the Bagni di Tivoli survey area. The investigation polygon (red) is overlaid on regional geological units from the CARG Lazio WMS, including anthropogenic deposits, volcanic products (lavas and tuffs), recent alluvial deposits, and travertines (blue hatched pattern). Data source: Regione Lazio Geoportal, CARG – Carta Geologica (WMS, accessed 2025).

2.3.2 Objectives and survey configuration

Industrial microgravity was applied to detect travertine-hosted cavities in advance of the Tiburtino hospital construction. Data acquisition was carried out in two distinct phases reflecting logistical constraints and site evolution. The first phase, conducted between July and August 2022, comprised 788 microgravity stations, while a second phase in February 2023 added 462 stations. Different base stations were adopted in the two phases for operational reasons; accordingly, the corresponding base-station datasets are treated as belonging to two independent surveys and analysed separately in this study, each representing a time-dependent experiment within a thermally and hydrogeologically active urban environment.

The survey was conducted on a regular 8 × 8 m grid covering approximately 50,000 m² (Figure 11), for a total of 784 gravity stations. The base, located outside the construction zone, was visited 2–3 times per day. Positioning was obtained by GNSS/RTK and heights converted to orthometric elevations using IGM geoid grids [29]. A summary of acquisition parameters is reported in Table 5

Figure 11. Orthophoto of the microgravity survey site showing the investigation area and measurement layout. Phase 1 gravity acquisition points are displayed in orange, while additional acquisition points are shown in yellow, arranged on a regular 8 × 8 m grid covering approximately 50,000 m².

Table 5. Field acquisition summary — Bagni di Tivoli (Rome, Italy).

Item	Details
Site	Bagni di Tivoli, Rome, Lazio, Italy
Acquisition period	July 2022 -February 2023
Industrial microgravity target	Travertine-hosted cavities / density heterogeneities in a hydrothermal setting
Operational objective	Reconnaissance of shallow voids/soft zones in a thermal-travertine context
Dominant lithology	Travertine bodies and Quaternary cover (hydrothermal carbonates)
Topographic instrument	Leica GS15 and Leica S1200 (GNSS/RTK)
Gravity instrument	Scintrex CG-5 Autograv
Total number stations phase 1	788
Total number stations phase 2	462
Station spacing	8 m (regular grid)
Acquisition parameters	60 s – 6 Hz

2.3.3 Analysis of raw base-station data

At Bagni di Tivoli, the base-station record comprises two distinct acquisition phases characterized by different temporal extents and operational conditions. The first phase, acquired between July and August 2022, spans approximately 40 days and is shown in Figure 12. The second phase, collected in February 2023, covers a shorter interval of approximately 8 days and is shown in Figure 13. Each phase includes the full set of base-station reoccupations and is treated as an independent temporal series.

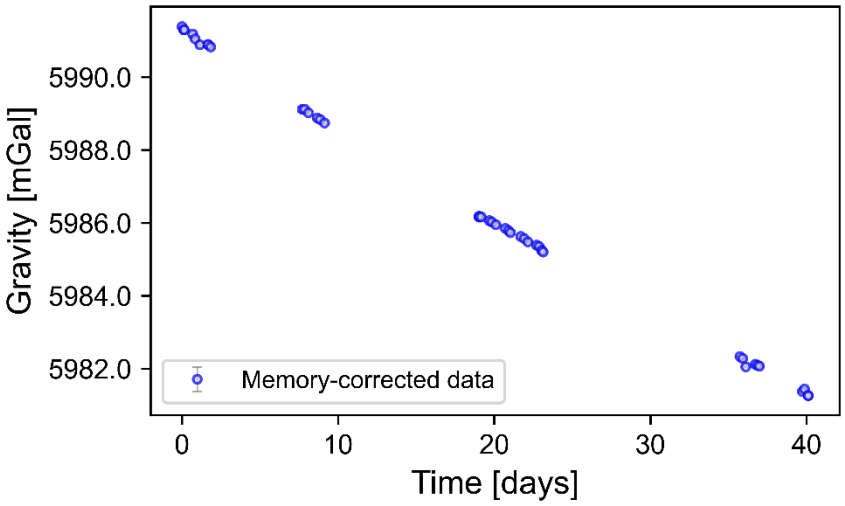

Figure 12. Temporal evolution of the base-station gravity measurements acquired during the first survey phase (July–August 2022), spanning approximately 40 days. The series shows a stable long-term trend with smooth, low-amplitude departures and limited short-term variability, consistent with environmental noise and instrumental response under field conditions.

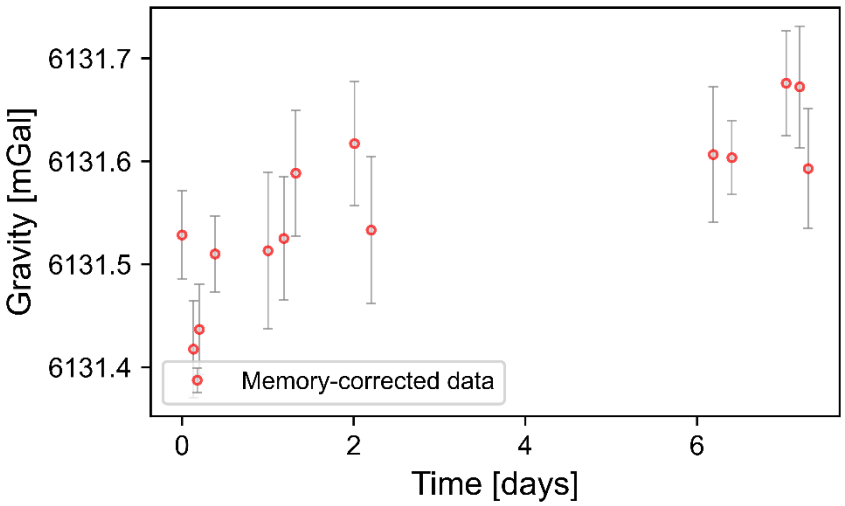

Figure 13. Temporal evolution of the measured gravity values during the acquisition period. The plot shows a stable trend with moderate short-term variability, consistent with environmental noise and instrumental response under field conditions.

At Bagni di Tivoli, the CG-5 standard deviation per 60-s reading quantifies the short-period noise affecting each gravity acquisition, as it reflects the variability of the 1-s corrected samples within individual readings. The SD distributions for the two survey phases are shown in Figure 14 and Figure 15, with the corresponding statistical parameters reported in Table 6 and Table 7.

During the first acquisition phase (July–August 2022), SD values are relatively low and compact (Figure 14), with a median of 31 µGal and a mean of 33 µGal over 41 readings (Table 6), indicating stable short-term conditions. In contrast, the second phase (February 2023) exhibits systematically higher and more dispersed SD values (Figure 15), with a median of 58.5 µGal and a mean of 55 µGal over 14 readings (Table 7), pointing to significantly less stable short-term conditions.

This difference is plausibly attributed to varying environmental noise levels: reduced heavy-vehicle traffic on the nearby motorway during the summer period likely contributed to lower short-period noise, whereas increased traffic intensity and ongoing construction activity in February enhanced anthropogenic microvibrations and within-reading scatter.

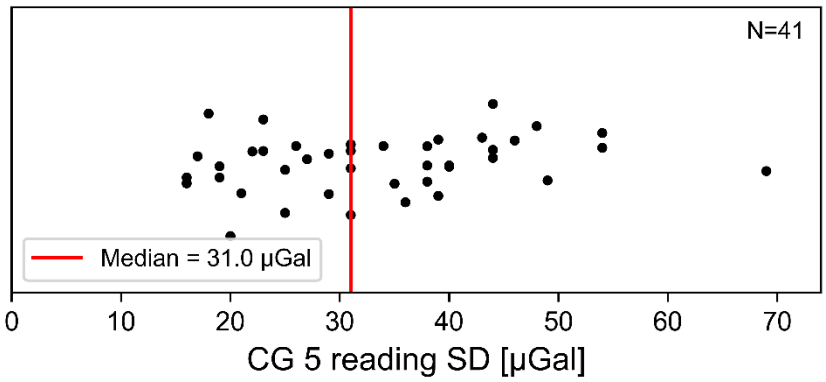

Figure 14. Bagni di Tivoli phase 1—CG-5 SD per 60-s reading (standard deviation of 1-s corrected samples); each marker is one reading; red line: median.

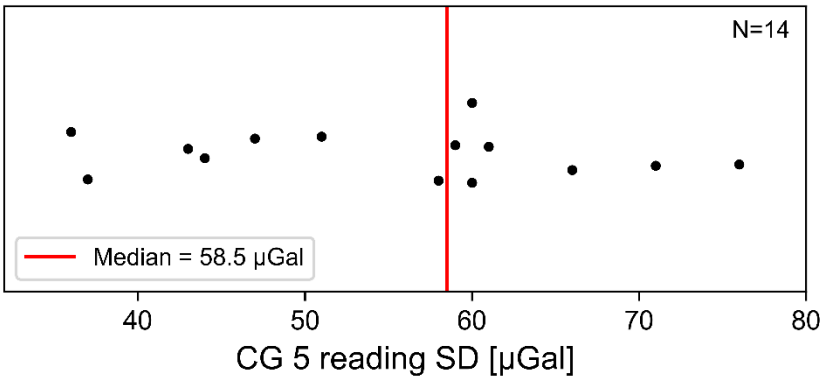

Figure 15. Bagni di Tivoli phase 2—CG-5 SD per 60-s reading (standard deviation of 1-s corrected samples); each marker is one reading; red line: median

Table 6. Statistical parameters describing the quality and stability of the base-station dataset acquired at Bagni di Tivoli in phase 1.

Parameter	Value / Observation
Number of readings	41
Mean SD (μGal)	33
Median SD (μGal)	31
Standard deviation SD (μGal)	12
Minimum SD (μGal)	16
Maximum SD (μGal)	69
Memory resets detected	/

Table 7. Statistical parameters describing the quality and stability of the base-station dataset acquired at Bagni di Tivoli in phase 2.

Parameter	Value / Observation
Number of readings	14
Mean SD (μGal)	55
Median SD (μGal)	59
Standard deviation SD (μGal)	12
Minimum SD (μGal)	36
Maximum SD (μGal)	76
Memory resets detected	/

2.4 Fujairah (UAE)

2.4.1 Geological and environmental setting

The study area is located in the northern sector of the Oman–UAE Mountains, within the Semail Ophiolite belt, one of the best-exposed oceanic lithosphere sections worldwide (Figure 16). The near-surface geology is dominated by ultramafic and gabbroic units of the ophiolitic crust, locally juxtaposed with fractured carbonate platforms of the Musandam Group and discontinuous alluvial deposits [30], [31], [32]. These lithologies exhibit strong lateral and vertical density contrasts, which motivated the original application of microgravity for mineral exploration.

From the perspective of this thesis, the relevance of the site lies primarily in its environmental and operational conditions: rugged topography, strong relief, arid climate, and large daily thermal excursions. These factors subject the gravimeter to substantial mechanical and thermal loading without implying genuine temporal mass variations at the base-station location, thereby providing a demanding test case for instrument-related temporal bias under desert environmental conditions.

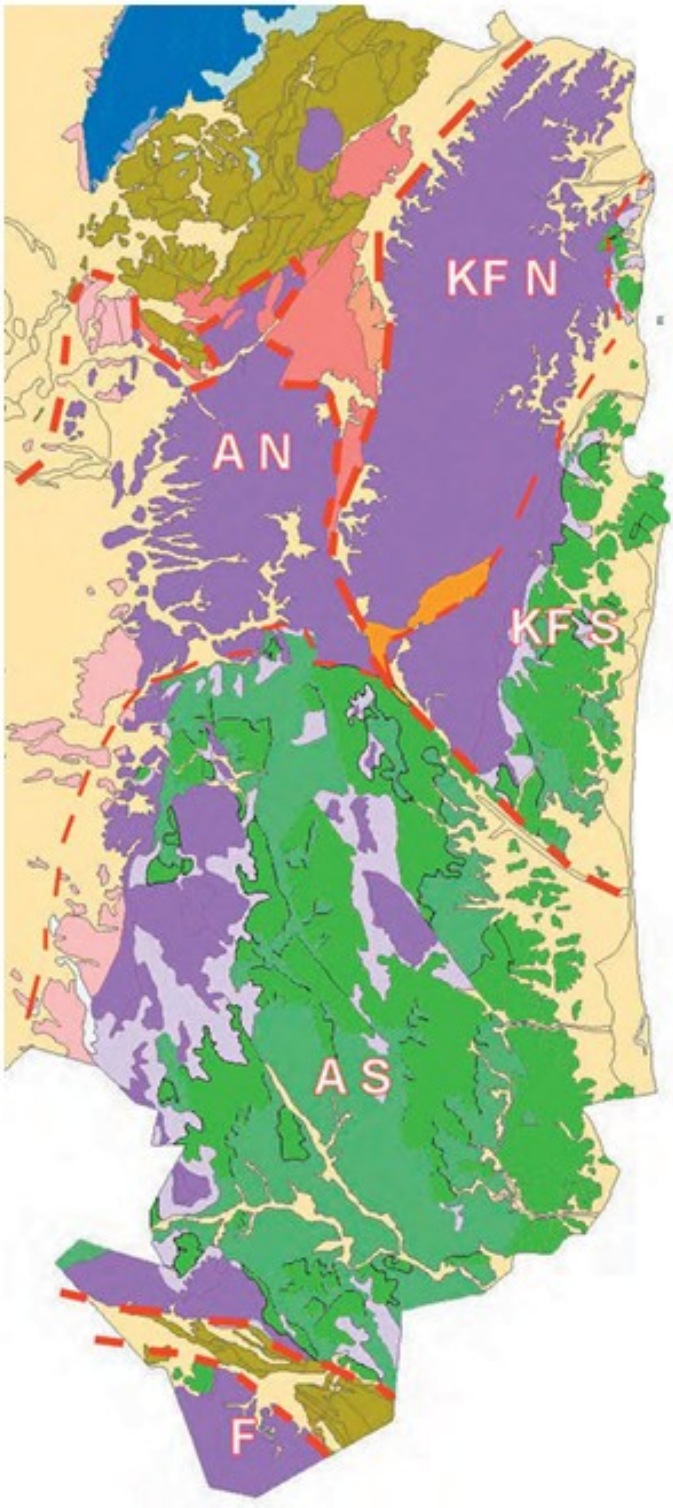

Figure 16 Simplified geological map of the Semail Ophiolite in the UAE. block abbreviations: KFN = Khor Fakkan North, KFS = Khor Fakkan South, AN = Aswad North, AS = Aswad South, F = Fizh. mantle harzburgite = dark purple; mixed unit = light purple; early crustal rocks = bright green; later crustal rocks = dark green. thrusts = thick red lines; internal shears = thin red lines. non-ophiolitic rocks: carbonates (blue), foreland sediments (brown), metamorphics (pink–orange), Quaternary deposits (beige) [31].

2.4.2 Objectives and survey configuration

The Fujairah campaign supported mineral exploration by detecting density contrasts associated with intrusive gabbroic bodies within the ophiolitic sequence. Within this thesis, the dataset is reinterpreted as a long-duration time-dependent experiment based on repeated gravity measurements at a fixed reference station, acquired under harsh desert–mountain conditions. Data acquisition was conducted between December 2023 and April 2024 over several sub-areas, covering a total extent of approximately 16 km² (Figure 17). Gravity measurements were collected on regular grids with 50 m spacing using a Scintrex CG-5 Autograv, with 30 s integration time at 6 Hz sampling. The base station on a bedrock outcrop was reoccupied twice daily throughout the 3-month campaign. Topographic positioning was performed using a GNSS base–rover configuration, with a Leica GS15 receiver operating as the base station and a Leica GS14 receiver used as rover (Figure 18), providing centimetric-level positioning for all gravity stations. The gravimeter was transported daily by vehicle and on foot across steep and exposed terrain, while ambient temperatures frequently exceeded 35–40 °C. A summary of acquisition parameters is reported in Table 8.

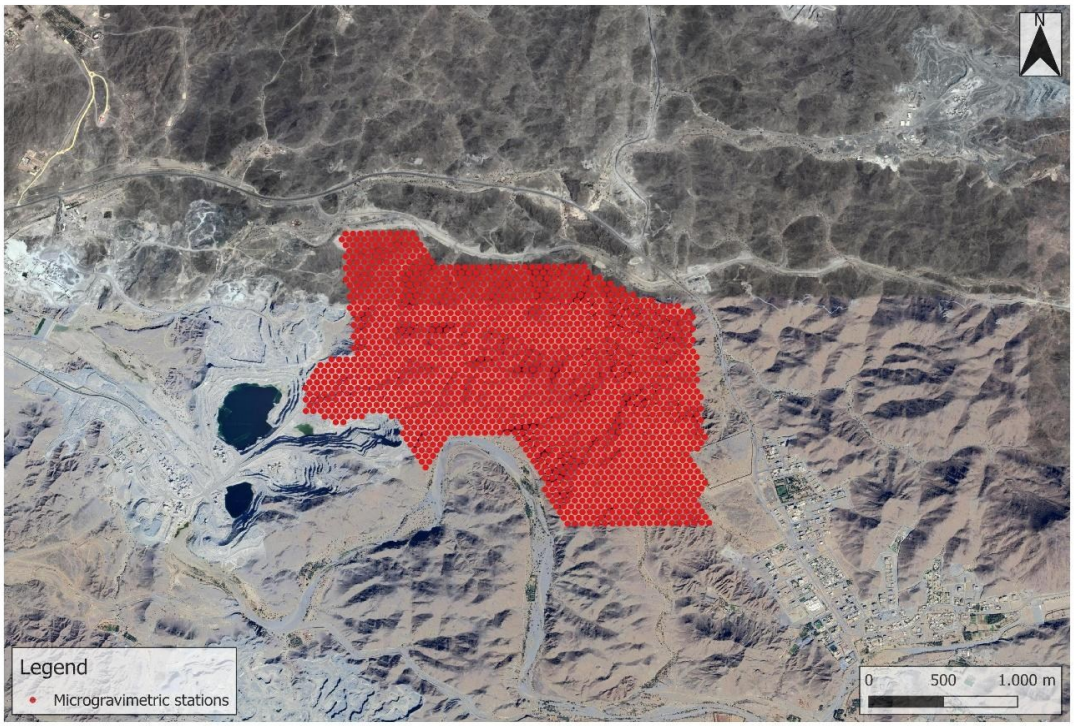

Figure 17. Microgravity survey polygon in the UAE study area, showing the spatial extent of the acquisition zone (~16 km²) and the distribution of gravity stations (red) across mountainous and alluvial domains.

Figure 18. Leica GS15 base station setup in the UAE survey area. Installation of the Leica GS15 GNSS receiver at the highest morphologic point to ensure optimal radio link coverage with the rover GS14 during the topographic survey operations. The elevated positioning minimized signal obstruction across the rugged volcanic terrain.

Table 8. . Field acquisition summary — Fujairah–Ras Al Khaimah (UAE).

Item	Details
Site	Fujairah–Ras Al Khaimah sector, northern Oman–UAE Mountains
Acquisition period	December 2023 – April 2024
Industrial microgravity target	Density contrasts associated with intrusive “younger gabbro” tongues in the Semail Ophiolite
Operational objective	Mineral exploration support; screening for gabbroic bodies via density mapping
Dominant lithology	Ophiolitic crust (layered/upper gabbros; ultramafics) with local carbonate/alluvial cover
Topographic instrument	Leica GS15 (base) + Leica GS14 (rover)
Gravity instrument	Scintrex CG-5 Autograv
Total number stations	1600
Station spacing	50 m (regular grid)
Acquisition parameters	30 s – 6 Hz

2.4.3 Analysis of raw base-station data

The base-station series acquired during the Fujairah–Ras Al Khaimah campaign spans more than three months, documenting the temporal evolution of CG-5 readings under desert environmental conditions. Figure 19 shows a sequence of measurement intervals separated by instrument resets. Between resets, the series evolves smoothly over time, whereas the transitions between intervals appear as step-like offsets. Over the full record, these discontinuities control much of the long-term behaviour and are best interpreted as operational artefacts rather than as changes driven by the local environment.

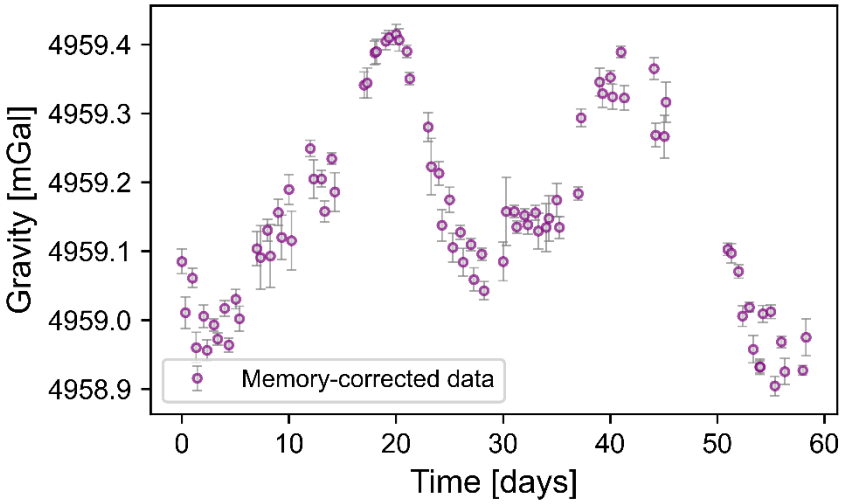

Figure 19. Gravity time series at the Fujairah base station. Step changes separate acquisition segments corresponding to memory resets.

The Fujairah base station provides the most favorable short-term noise conditions in the dataset, as shown by the CG-5 SD per reading (30 s integration) in Figure 20 and Table 9. SD values are predominantly low, with median = 15 µGal and mean = 17 µGal over n = 101 readings, indicating excellent within-reading stability for most of the campaign. The distribution nevertheless exhibits a clear upper tail (up to 49 µGal), which is compatible with intermittent environmental forcing typical of open desert operations (e.g., wind-induced vibration, occasional nearby activity, or temporary suboptimal coupling/levelling). Four memory resets are present and are handled as step offsets in preprocessing; the SD statistics remain consistent with an overall low-noise site punctuated by a limited number of noisier intervals.

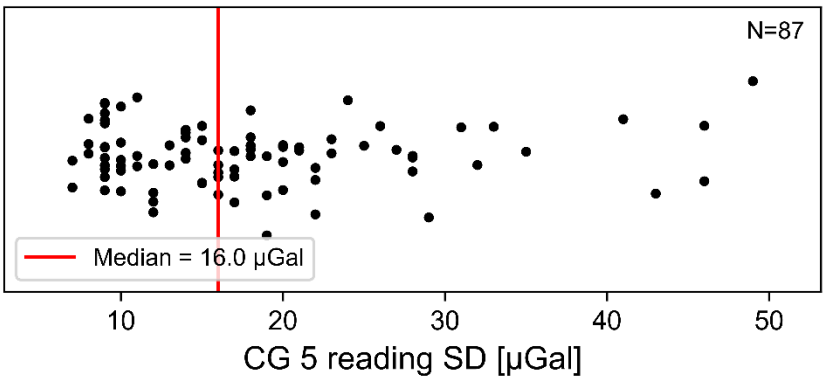

Figure 20. Fujairah base station: CG-5 SD per reading (30 s integration). Low median SD indicates excellent short-term stability; occasional higher SD readings reflect intermittent environmental forcing. Red line: median.

Table 9. Statistical parameters describing the quality and stability of the base-station dataset acquired at Fujairah.

Parameter	Value / Observation
Number of readings	87
Mean SD (µGal)	17
Median SD (µGal)	16
Standard deviation SD (µGal)	9
Minimum SD (µGal)	5
Maximum SD (µGal)	49
Memory resets detected	4

2.5 Rio Marina (Elba Island, Italy)

2.5.1 Geological and environmental setting

The Rio Marina site is located in the eastern sector of Elba Island, within the Northern Apennine structural domain, at the tectonic contact between the Gràssera Unit and the Ligurian–Piedmont Ophiolitic Unit [21], [22] (Figure 21-Figure 22). This contact is expressed as a highly deformed tectonic mélange, where strongly sheared metamorphic pelites are juxtaposed with serpentinized ultramafics, basalts, radiolarites, and cherty limestones. The resulting litho-structural framework is characterized by steeply dipping units, intense fracturing, and sharp lateral density contrasts at shallow depth.

The area hosts Fe–Mn mineralizations associated with hydrothermal and metasomatic processes, extensively exploited until the late twentieth century. Abandoned open pits, waste dumps, and mining-related voids are widespread, producing a complex anthropogenic overprint superimposed on an already heterogeneous geological setting. Quaternary alluvial, colluvial, and slope-wash deposits locally infill fault-controlled depressions, where differential compaction and dissolution processes favour sinkhole development (Figure 23).

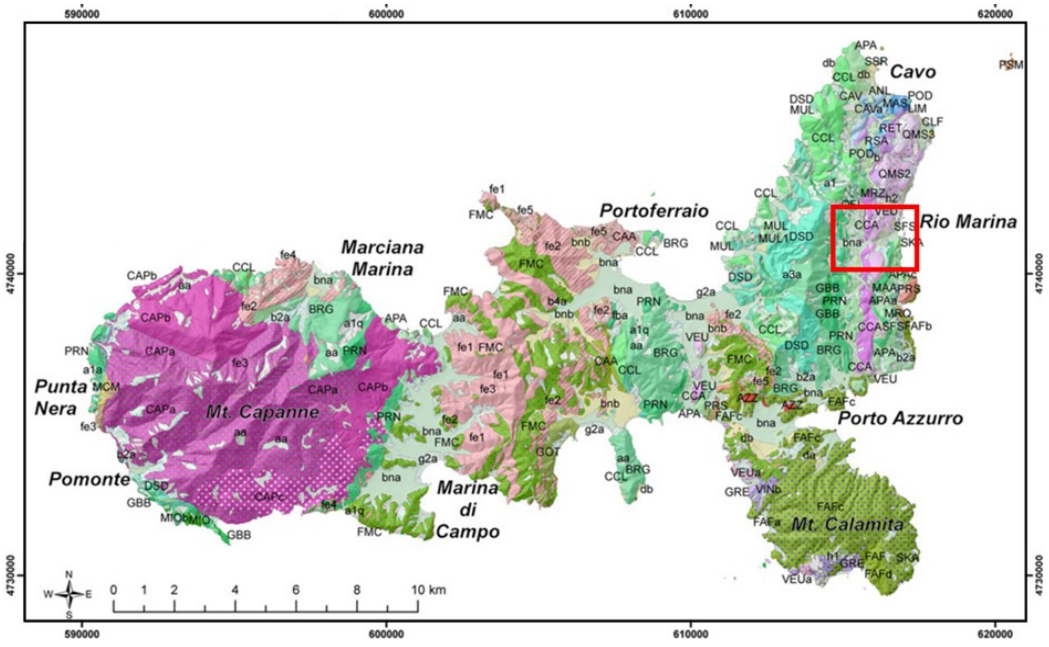

Figure 21. Geological map of Elba Island. The western sector is dominated by intrusive rocks (magenta), while the central and eastern sectors show metamorphic and ophiolitic lithologies (green, violet, and red). The red box indicates the Rio Marina study area.

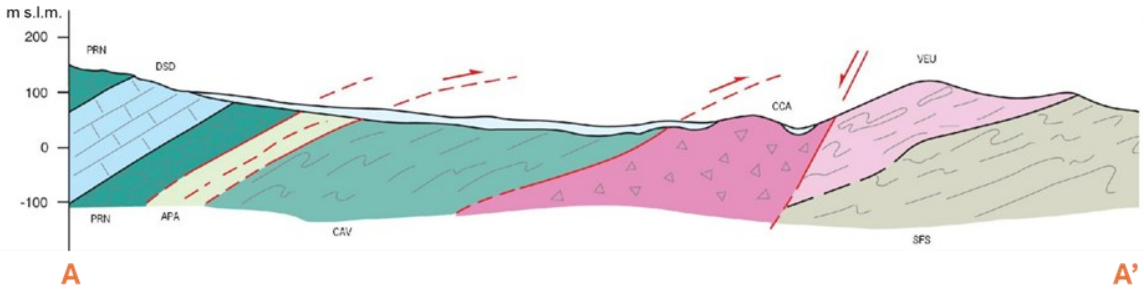

Figure 22. Geological section A–A' across the Valle dei Mulini [33], illustrating the structural superposition of the Ophiolitic and Gràssera Units.

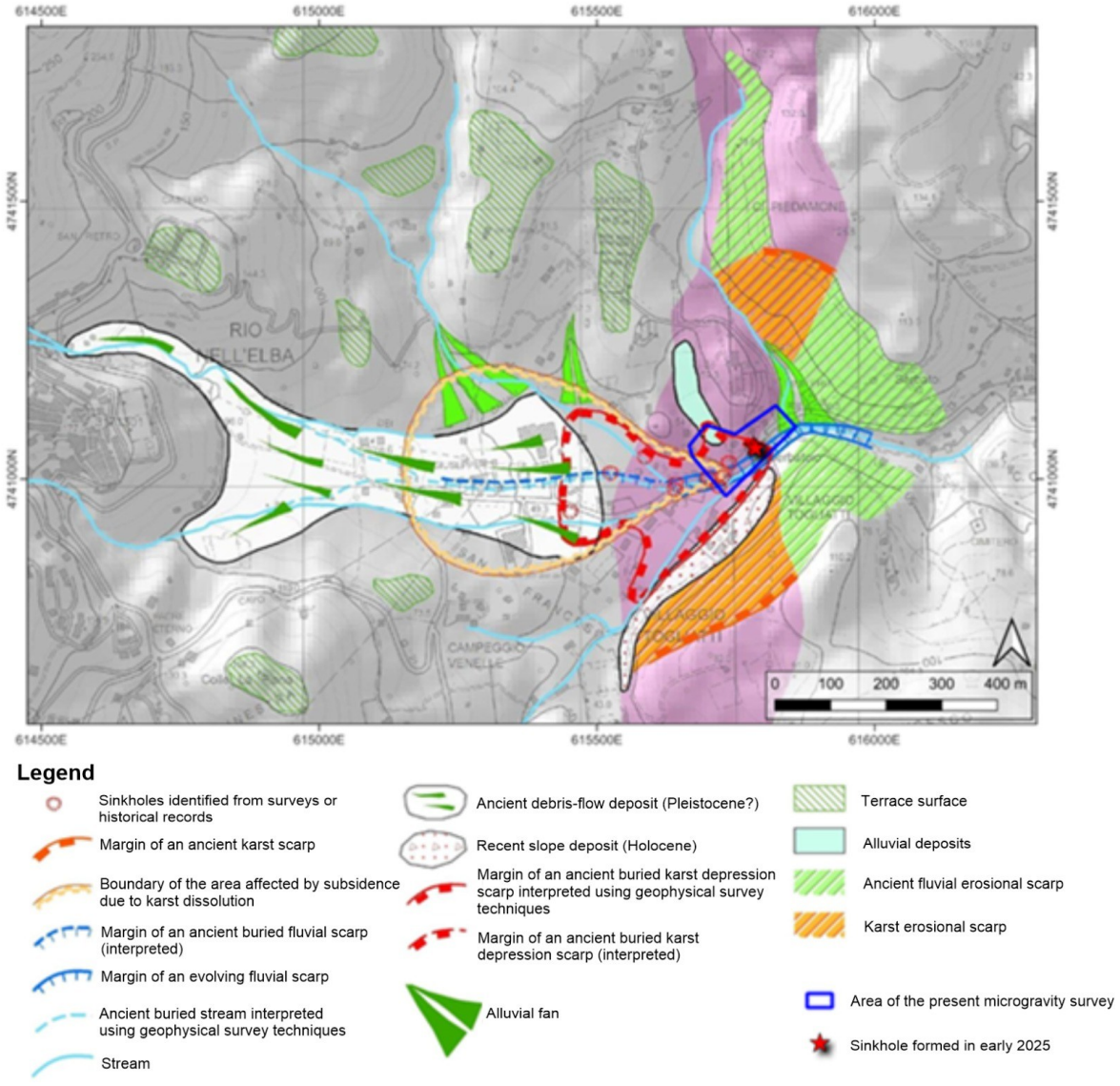

Figure 23. Geomorphological–dynamic map of the Rio Marina area [33], showing Quaternary deposits, fault traces, and locations of sinkholes identified up to 2025.

2.5.2 Objectives and operational framework

The microgravity survey at Rio Marina was initiated following the sudden formation of a sinkhole affecting a secondary road and adjacent areas in the Valle dei Mulini sector in April 2025 (Figure 24). The primary applied objective was to delineate zones of shallow instability associated with cavernous limestone dissolution and to assess the potential for further sinkhole development.

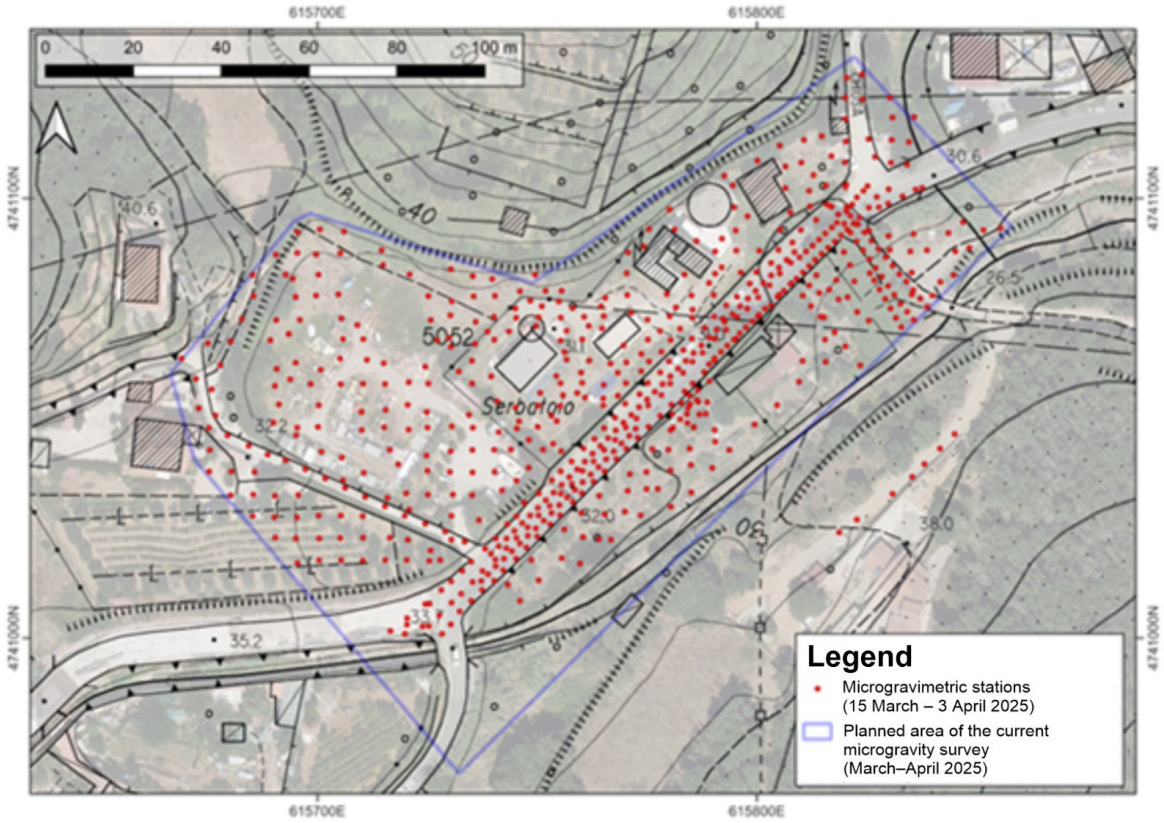

Figure 24. Layout of the Rio Marina survey grid showing the irregular spacing pattern

The acquisition was conducted over a three-week period, providing repeated gravity measurements at a fixed reference station under stable meteorological conditions and limited anthropogenic disturbance. This temporal extent allows the analysis of systematic variability in repeated CG-5 observations at a physically invariant location, independently of true subsurface mass changes.

The survey covered approximately 250,000 m² around the sinkhole depression (Figure 6). Station spacing was adapted to the expected deformation pattern, ranging from ~1 m within the active subsidence zone to ~3–5 m in surrounding areas.

A single base station was installed on mechanically stable ground outside the active karst area and reoccupied 4–5 times per day to ensure dense temporal control. A summary of the acquisition parameters is reported in Table 10.

Table 10. Field acquisition summary — Rio Marina (Elba Island, Italy).

Item	Details
Site	Rio Marina, Elba Island, Italy
Acquisition period	March 2025
Industrial microgravity target	Shallow cavities/low-density zones associated with active/sub-recent sinkhole processes
Operational objective	Map additional evidence of sinkhole-related instability beyond the collapse area
Dominant lithology	Metamorphic bedrock and coastal cover; urban/road embankment materials locally
Topographic instrument	Leica GS15 + total station Leica MS50
Gravity instrument	Scintrex CG-5 Autograv
Total number stations	660
Station spacing	Irregular: 1 m in the subsidence core, grading to ~5 m outward
Acquisition parameters	30 s – 6Hz

2.5.3 Analysis of raw base station-data

The raw gravity time series acquired at Rio Marina (Figure 25) compiles the measurements collected during the campaign and shows a clear day-scale pattern superimposed on the longer-term evolution. Within the main measurement windows, the signal follows a smooth temporal progression without step-like jumps that would indicate memory-reset discontinuities, supporting the interpretation of continuous acquisition segments.

Beyond the overall trend, the record exhibits a pronounced repeatable daily structure, with quasi-periodic intra-day fluctuations recurring across successive days. The absence of reset-driven steps within segments makes the dataset suitable for characterising instrument-related temporal variability and for testing harmonic representations of the deterministic component.

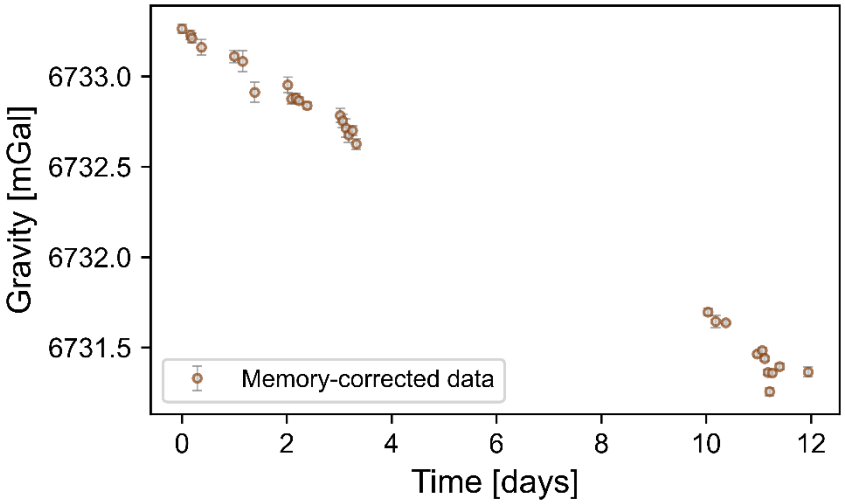

Figure 25. Gravity time series acquired at the Rio Marina base station during the survey.

The structure of the signal thus represents a high-quality temporal dataset in which instrumental and exogenous components cannot yet be separated. At this stage the signal shape is kept in raw form; quantitative interpretation is deferred to Chapter 3.

Short-term measurement stability at Rio Marina is described through the CG-5 reading SD (60-s integrations), i.e., the standard deviation of the 1-s gravity estimates derived from the 6-Hz signal within each reading. The SD dot-plot (Figure 26), yields a median of 26 µGal, with a wide range (9–58 µGal, Table 11), indicating moderate noise with intermittent excursions to higher SD.

The presence of higher-SD readings suggests a disturbance conditions rather than a stationary noise floor. In addition to intermittent surface activity and exposure-related micro vibrations, the local setting may contribute significantly: the proximity of a well-field area and the associated dense network of buried utilities can introduce persistent low-amplitude vibrations (e.g., pump cycling, fluid/pressure transients, and infrastructure-borne mechanical noise) that increase the within-reading scatter captured by the CG-5 SD.

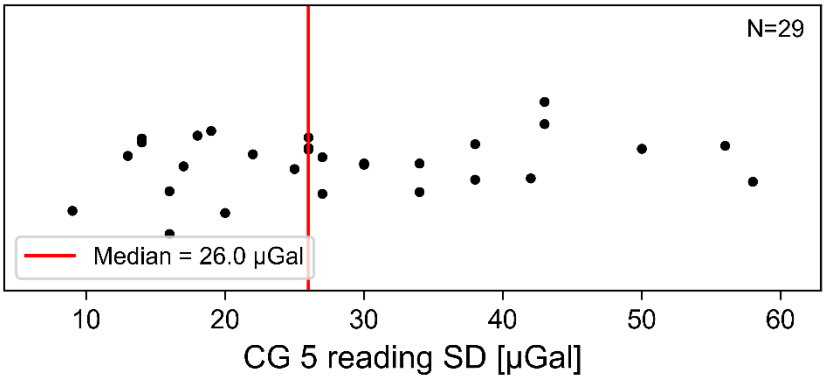

Figure 26. Rio Marina base station—CG-5 reading SD for each 60-s reading; red line marks the median.

Table 11. Statistical parameters describing the quality and stability of the base-station dataset acquired at Rio Marina.

Parameter	Value / Observation
Number of readings	38
Mean SD (µGal)	29
Median SD (µGal)	26
Standard deviation SD (µGal)	13
Minimum SD (µGal)	9
Maximum SD (µGal)	58
Memory resets detected	/

2.6 Tivoli (Lazio, Italy)

2.6.1 Geological and environmental setting

The Tivoli survey area is located east of Rome along the Aniene valley, within the hydrothermal basin hosting the Tivoli Travertine Complex (Figure 27). The near-surface geology is dominated by porous, variably friable travertines (TBTC unit) precipitated from fault-controlled hydrothermal fluids, locally overlying more compact lithoid travertines and surrounded by volcanic tuffs and Quaternary alluvial deposits [25]. Fault-controlled permeability and heterogeneous porosity within the travertine body promote localized dissolution and mechanical weakening, producing sharp lateral density contrasts at shallow depth. These conditions define a favourable context for microgravity investigations aimed at detecting cavities and loosened zones, while also providing laterally stable sectors suitable for base-station installation where no true temporal mass changes are expected.

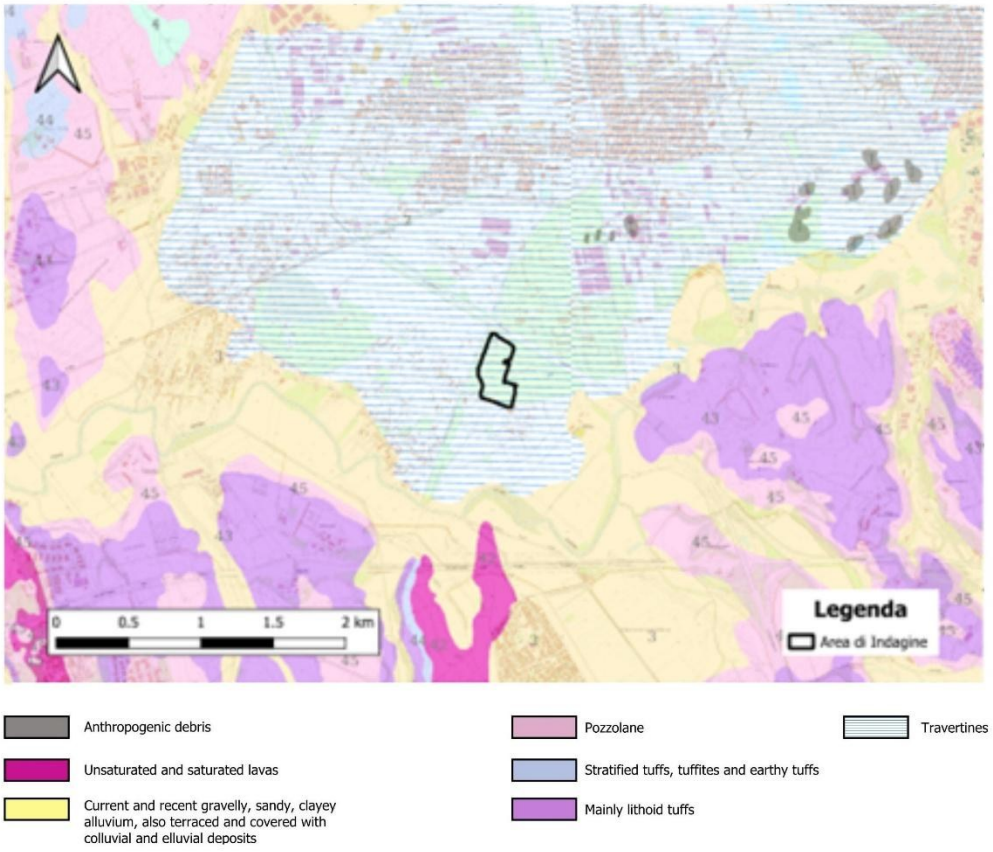

Figure 27. Geological framework of the Tivoli survey area, showing the investigation polygon (red) overlaid on regional geological units from the CARG Lazio WMS, including anthropogenic deposits, volcanic products (lavas and tuffs), recent alluvial deposits, and travertines (blue hatched pattern). Data source: Regione Lazio Geoportal, CARG – Carta Geologica (WMS, accessed 2025).

2.6.2 Objectives and operational framework

The microgravity survey was conducted in April 2025 within the Guidonia–Tivoli sector, adjacent to the A1 motorway, as part of preliminary investigations for planned logistics facilities. The applied objective was to exclude the presence of shallow cavities or density anomalies associated with sinkhole-prone travertine terrains, in compliance with regional guidelines for sinkhole risk assessment (DGR Lazio 1159/2002).

The acquisition extended over approximately two weeks and consisted of repeated gravity measurements referenced to a fixed base station, providing a dataset suitable for analysing systematic temporal variability of CG-5 observations under strong anthropogenic vibration. The site represents an urban–infrastructure setting where external low-frequency noise is persistent but spatially invariant, allowing separation between short-period measurement scatter and long-period instrumental drift.

The survey covered ~4500 m² and was organized on a regular 3 × 3 m grid optimized for accessibility constraints (Figure 28). A single base station was reoccupied three to four times per day to ensure temporal control. Station positioning was obtained using a Leica GS15 GNSS receiver in RTK mode, with heights converted to orthometric elevations using official IGM geoid grids. A synthesis of acquisition parameters and field conditions is reported in Table 12.

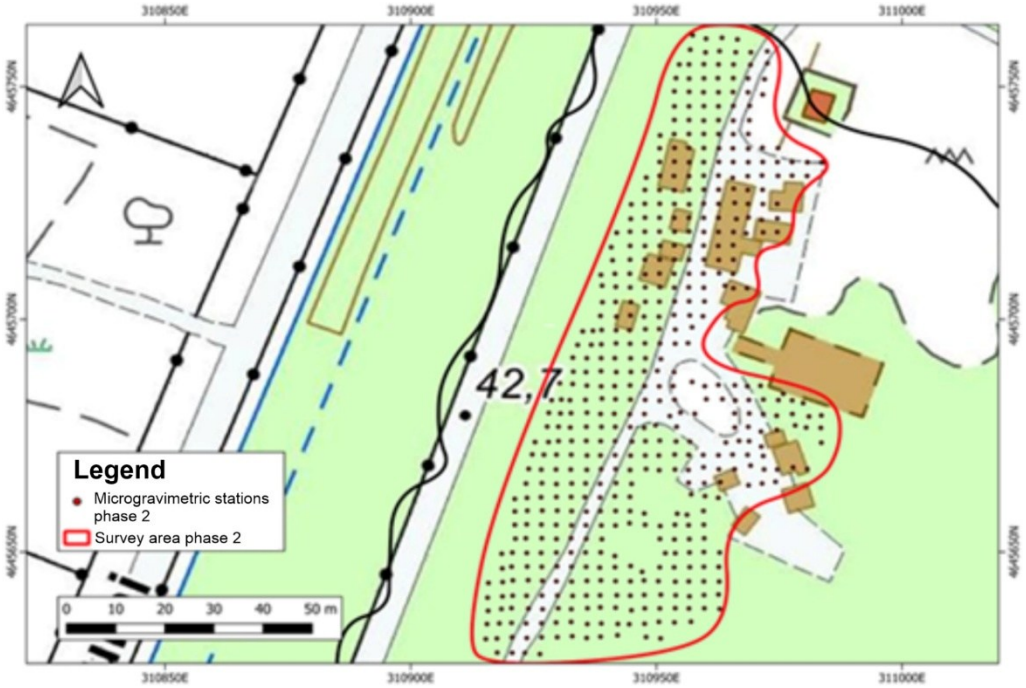

Figure 28. Location of microgravity stations and survey area (phase 2). Base map from the *Carta Tecnica Regionale Numerica della Regione Lazio v.2014*, scale 1:5000 (WGS84/UTM Zone 33N, EPSG:32633).

Table 12. Field acquisition summary — Tivoli (Rome, Italy).

Item	Details
Site	Guidonia–Tivoli sector near A1 motorway, Lazio, Italy
Acquisition period	April 2025
Industrial microgravity target	Sinkhole susceptibility screening for pre-construction risk mitigation
Operational objective	Exclude shallow voids ahead of logistics-hub building works in an area governed by regional sinkhole guidelines
Dominant lithology	Travertine bodies and Quaternary cover (hydrothermal carbonates)
Topographic instrument	Leica GS15, GNSS RTK
Gravity instrument	Scintrex CG-5 Autograv
Total number stations	680
Station spacing	3 m (regular grid over ~4500 m²)
Acquisition parameters	60 s – 6 Hz

2.6.3 Analysis of raw base-station data

Figure 29 compiles approximately nine days of Tivoli base-station reoccupations acquired in an urban setting affected by persistent vibration from traffic along the nearby A1 highway. The dataset is structured into daily measurement cycles, producing short clusters of observations separated by the intervals between successive reoccupations. The sequence remains internally consistent, with no step-like discontinuities that would indicate memory-reset events or setup-related offsets.

The temporal evolution is dominated by a low-frequency systematic bias, on which a clear day-scale pattern is superimposed. Similar intra-day structures recur across consecutive days, indicating a repeatable cyclic contribution that modulates the baseline behaviour and should be captured when modelling the deterministic component of the series.

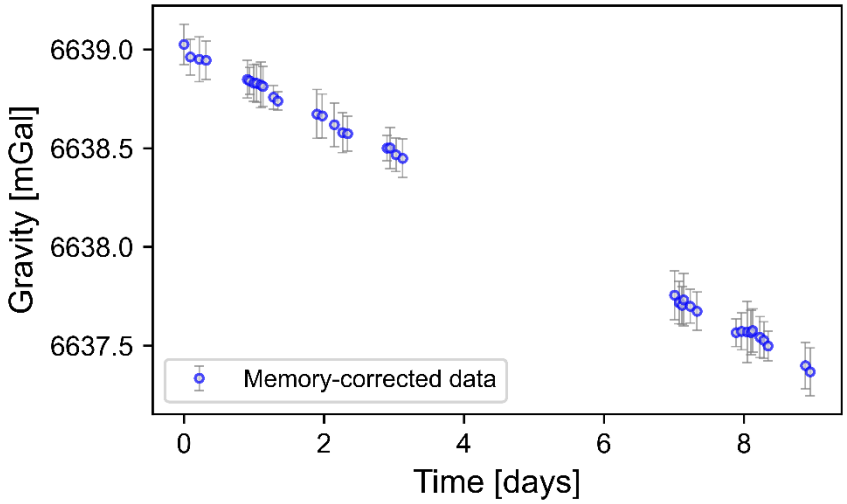

Figure 29. Gravity time series at the base station — Tivoli dataset. The time axis represents the continuous acquisition period, with reoccupations corresponding to daily operational cycles.

Tivoli is the noisiest base station in terms of per-reading SD among the surveyed sites (Figure 30; Table 13) SD is very high (median 98 µGal; mean 99 µGal; N=37) and ranges from 47 to 155 µGal. This behaviour is consistent with strong cultural noise, dominated by highway traffic–induced micro-vibrations that can efficiently couple into the instrument during integration.

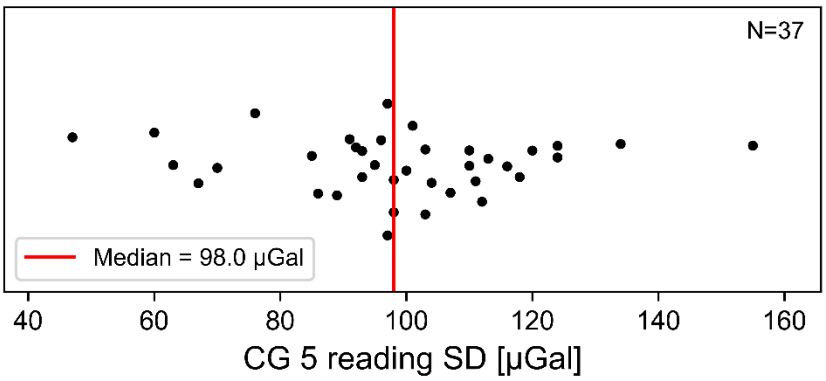

Figure 30. Tivoli base station: CG-5 per-reading SD for 60-s integrations (6-Hz sampling). Dots are readings; red line is the median; N is the number of readings.

Table 13. Statistical parameters describing the quality and stability of the base-station dataset acquired at Tivoli.

Parameter	Value / Observation
Number of readings	37
Mean SD (µGal)	99
Median SD (µGal)	98
Standard deviation SD (µGal)	21
Minimum SD (µGal)	47
Maximum SD (µGal)	155
Memory resets detected	/

2.7 Colle Mentuccia (Lazio, Italy)

2.7.1 Geological and environmental setting

The Colle Mentuccia site is located in the eastern sector of Rome, along Via Prenestina, on a low-relief surface of the Albani volcanic plateau. The geological framework is dominated by Pleistocene pyroclastic deposits of the Albano volcanic succession resting on the Pliocene Monte Vaticano clay unit, which acts as a regional aquiclude. Surface lithologies are mainly represented by welded ignimbrites (Tufo Lionato, VSN1) and overlying incoherent pozzolanic deposits (Pozzolanelle, VSN2), locally interlayered with thin distal stratified tuffs [25], [34].

At map scale, these units correspond to the CARG classes “mainly lithoid tuffs” and “pozzolane”, while valley bottoms host thin veneers of recent alluvium and colluvium (Figure 1). The volcanic succession is subhorizontal and laterally continuous, with no evidence of local faulting or karst-related cavity systems reported in the area. Hydrogeologically, shallow perched aquifers may develop within the pyroclastic sequence above the impermeable clay substratum, but no sinkhole clusters or documented underground voids are present [25], [26], [35].

This setting defines a mechanically stable urban plateau, characterized by limited geological heterogeneity at the survey scale and by the absence of expected subsurface mass changes, making the site suitable as a reference environment for assessing time-dependent instrumental effects.

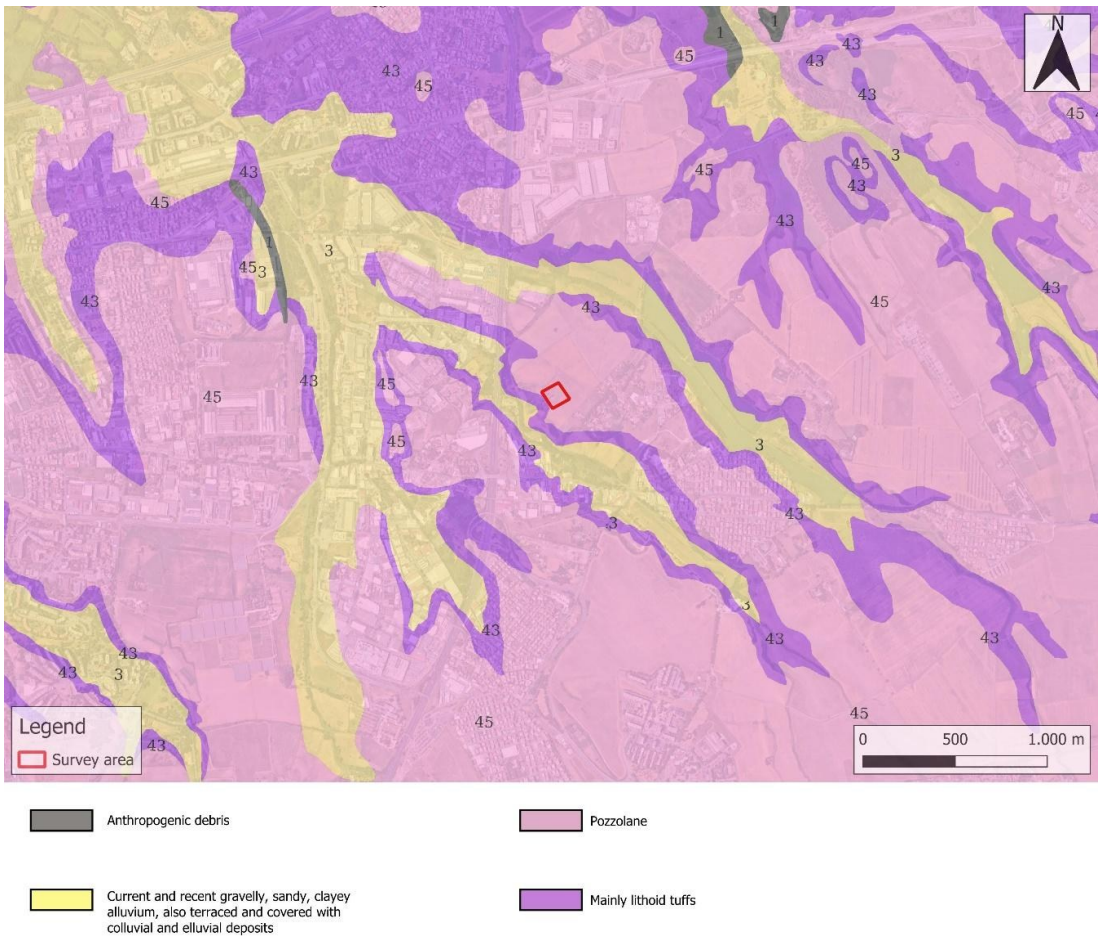

Figure 31. Geological framework of the Colle Mentuccia plateau map showing the survey area (red rectangle) overlaid on geological layers served via wms from the Regione Lazio geoportal (CARG Lazio). The legend highlights the main surface units: anthropogenic cuts and fills; active to recent drainage channels with sandy–gravelly deposits; mainly lithoid tuffs (≈ tufo lionato, vsn1) together with pozzolane (≈ pozzolanelle, vsn2, locally including pozzolane rosse/nere); thin lenses of stratified tuffs, tuffites and earthy tuffs (≈ distal sabatini, ltt). The plateau gently slopes sse–nnw toward the fosso di tor sapienza, from ~80 m to ~45 m a.s.l., conditioning shallow runoff and local infiltration. Data source: Regione lazio geoportal, wms "CARG — carta geologica" (accessed 2025).

2.7.2 Objectives and operational framework

The Colle Mentuccia microgravity survey was designed to investigate shallow ground instability in an urban context affected by anthropogenic cavities and reworked deposits, where repeated subsidence phenomena had been previously reported. The applied objective was the detection and spatial delineation of near-surface density deficits associated with underground voids and disturbed ground beneath paved surfaces and infrastructure.

Operationally, the survey acts as an urban-style dataset with repeated occupations over an extended period, useful for tracking time-dependent CG-5 behaviour. Station access was constrained by surface infrastructure, traffic limitations and fixed pavement geometry, resulting in a quasi-regular measurement layout adapted to local accessibility rather than an ideal grid. These constraints are representative of real engineering surveys, where operational regularity is subordinated to site conditions.

Measurements were organised along short linear profiles and small clusters covering the area of interest, with station spacing of approximately 1–2 m in zones suspected of subsurface instability. A single base station was installed on mechanically stable ground outside the suspected cavity zone and reoccupied multiple times per day to control temporal variability. The acquisition parameters and survey statistics are summarised in Table 14, while the spatial layout is shown in Figure 32.

Figure 32. Location of microgravity stations and survey area.

The repetition of base-station measurements over several weeks, combined with frequent reoccupation cycles within individual survey days, generates a time series suitable for isolating systematic temporal components in CG-5 readings at a physically invariant point. This configuration allows the separation of spatial gravity anomalies related to subsurface structure from time-dependent instrumental effects, making it suitable for testing drift-correction methods under realistic industrial constraints.

Table 14. Field acquisition summary — Colle Mentuccia (Rome, Italy).

Item	Details
Site	Colle Mentuccia (eastern Rome), Italy
Acquisition period	July 2025
Industrial microgravity target	Shallow density contrasts to inform a local hydrogeological model (utilities corridor present)
Operational objective	Provide density inputs/constraints for groundwater-related modeling and subsurface characterization
Dominant lithology	Albani volcanic pyroclastics (Pozzolanelle over Tufo Lionato)
Topographic instrument	Leica GS15 (RTK) + DJI Air 2S (orthophoto & DEM)
Gravity instrument	Scintrex CG-5 Autograv
Total number stations	250
Station spacing	Irregular 0.5 m on the main grid; additional transects spaced 5 m
Acquisition parameters	60 s – 6 Hz

2.7.3 Analysis of raw base-station data

The base-station time series acquired during the Colle Mentuccia survey (Figure 33) shows a smooth and monotonic decreasing trend over the observation period, with no discontinuities or step offsets. No reset-related steps are visible, consistent with uninterrupted memory handling during the campaign. The overall trend is dominated by a gradual drift, which will be quantitatively analysed in Chapter 3 to distinguish the instrumental component from possible environmental contributions.

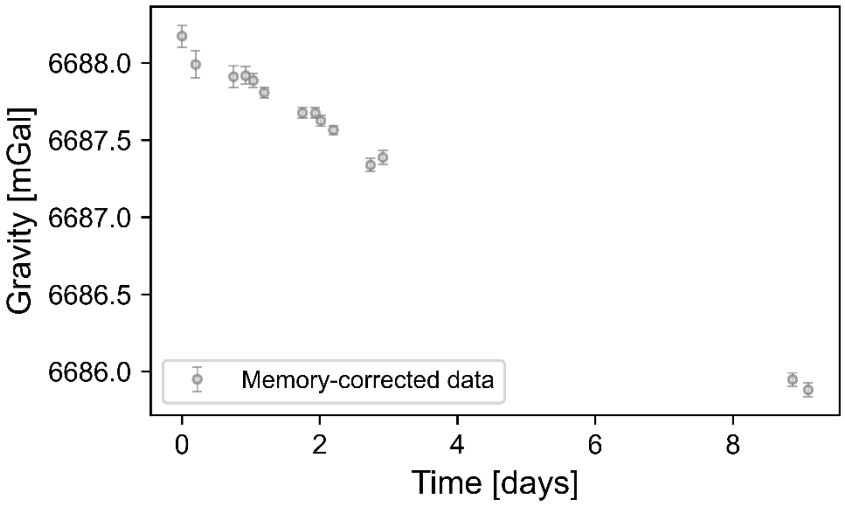

Figure 33. Gravity time series for the Colle Mentuccia base station.

SD indicates moderate scatter, with median 44 μGal (Figure 34; Table 15). Most readings cluster between ~30 and ~45 μGal, indicating reasonably stable conditions at the base station, while a limited number of higher-SD readings extend the range up to ~90 μGal. These elevated values are interpreted as local, short-lived perturbations plausibly associated with the presence of buried aqueduct pipelines, which may generate vibrational noise during intermittent flow variations or operational transients. Despite this upper tail, the dataset remains internally consistent, and the overall SD statistics fall within the typical operating range for industrial microgravity acquisition.

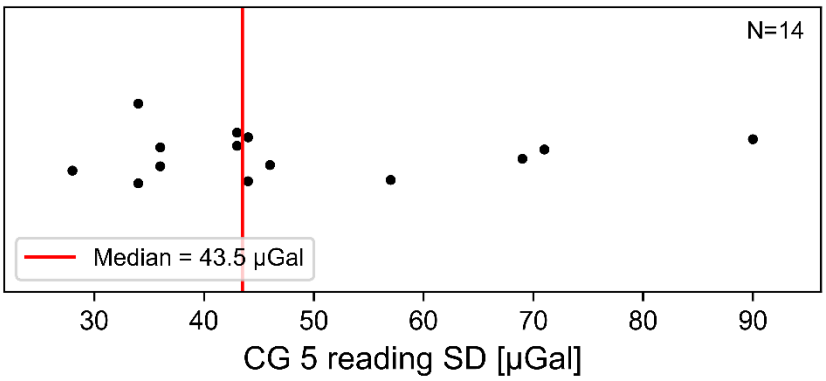

Figure 34. Colle Mentuccia base station—CG-5 internal SD per reading. Red line: median; N = 14.

Table 15. Statistical parameters describing the quality and stability of the base-station dataset acquired at Colle Mentuccia.

Parameter	Value / Observation
Number of readings	14
Mean SD (µGal)	48
Median SD (µGal)	44
Standard deviation SD (µGal)	17
Minimum SD (µGal)	28
Maximum SD (µGal)	90
Memory resets detected	/

2.8 San Giovanni laboratory test (Tuscany, Italy)

A continuous acquisition test was carried out at the Centro di Geotecnologie laboratory in San Giovanni Valdarno in order to characterise the intrinsic short-term stability and temporal behaviour of the CG-5 gravimeter under controlled environmental conditions. The instrument was operated indoors, on a stable concrete floor, with no intentional mechanical disturbance and under quasi-constant temperature conditions (Figure 35).

Figure 35. Location of the CG-5 continuous gravity station at the Centro di Geotecnologie, San Giovanni Valdarno, and photograph of the instrument setup during laboratory acquisition.

The gravimeter acquired continuously for approximately 21 days, producing a high-density base-station time series that can be regarded as free from significant operational forcing. In this configuration, gravity variations are expected to reflect only instrumental response and low-level environmental noise, providing a reference dataset for comparison with field-acquired base-station records. The temporal evolution of the gravity signal is shown in Figure 36, where the memory-corrected gravity values form a smooth, continuous time series with no step-like discontinuities.

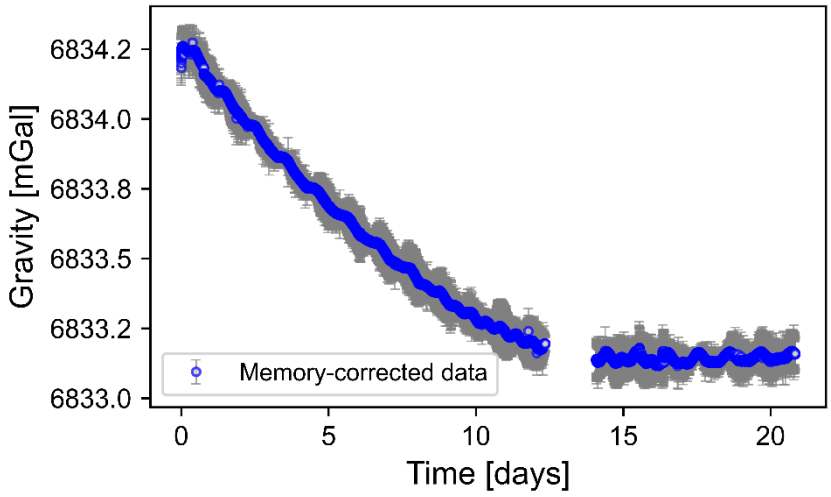

Figure 36. Temporal evolution of gravity values recorded during the 21-day continuous acquisition test at the Centro di Geotecnologie laboratory (San Giovanni Valdarno). Data are shown after correction for tidal effects. Error bars represent the within-reading standard deviation.

Short-period noise was quantified through the standard deviation of the 1-s corrected samples within each 60-s reading. The distribution of CG-5 reading SD values is shown in Figure 37, based on a total of N = 25069 readings. The SD values cluster around a median of 42 µGal, with limited dispersion and no evidence of bimodality or episodic noise bursts.

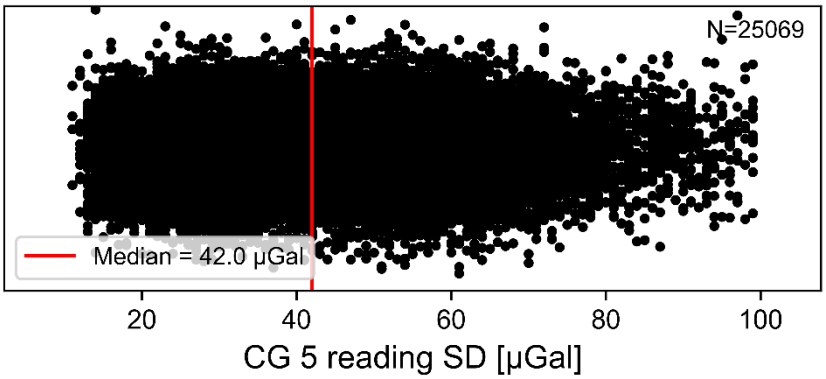

Figure 37. Distribution of CG-5 reading standard deviation (SD) for 60-s integrations during the continuous acquisition test. Each marker represents one reading (*N = 25069*). The red vertical line indicates the median SD value.

The main statistical parameters describing the quality and stability of the dataset are summarised in Table 16. The relatively narrow SD distribution and the absence of memory resets indicate that, under controlled laboratory conditions, the CG-5 exhibits stable short-term performance and a well-behaved temporal response. This dataset therefore provides a benchmark for interpreting the additional variability observed in field base-station records, where environmental and operational factors are superimposed on the intrinsic instrumental behaviour.

Table 16. Statistical parameters describing the quality and stability of the base-station dataset.

Parameter	Value / Observation
Number of readings	25069
Mean SD (μGal)	44
Median SD (μGal)	42
Standard deviation SD (μGal)	16
Minimum SD (μGal)	11
Maximum SD (μGal)	99
Memory resets detected	/

3 Harmonic correction of CG-5 temporal bias

Microgravity surveys were carried out using Scintrex CG-5 relative gravimeters operated at microgal precision under heterogeneous environmental and industrial conditions, encompassing urban, peri-urban and natural settings with contrasting operational constraints [2], [8], [36]. The analysis in Chapter 2 shows that, even at fixed base stations and after internal Longman-type tidal correction, CG-5 gravity records exhibit systematic, non-random temporal variability whose amplitude is often comparable to that of the target anomalies, thereby challenging standard linear drift assumptions commonly adopted in applied surveys [4], [7], [8].

Current practice typically addresses drift through empirical corrections, such as linear trends applied over daily or campaign-scale windows, or low-order polynomial detrending selected on the basis of residual statistics [7], [8], [12], [15], [19]. Although these approaches can be effective within restricted temporal windows, they are inherently dependent on segmentation choices and operator decisions, and do not explicitly reflect the dynamic response of the CG-5 as a spring-based, feedback-controlled system. As a result, their applicability and stability across surveys of different duration and noise conditions remain limited.

This chapter presents a unified, physically motivated framework for modelling and correcting the deterministic component of systematic temporal bias in CG-5 base-station time series. All base-station records acquired between 2021 and 2025 at the sites described in Chapter 2, together with a long-duration benchmark experiment at San Giovanni Valdarno, are analysed using a single standardized workflow. After quality control based on reading standard deviation and correction of offsets associated with memory handling, each continuous segment is modelled by a multi-harmonic formulation estimated through weighted least squares.

Harmonic components are selected automatically within constrained low- and high-frequency period ranges consistent with the instrument temporal response, while amplitudes, phases and constant offsets are estimated by weighted least squares. Model performance is assessed using reduced χ^2 statistics and residual dispersion, and compared with conventional linear and polynomial drift corrections applied to the same datasets.

The objective of this chapter is to assess whether a compact harmonic representation can reliably isolate and remove the deterministic component of CG-5 base-station variability, reducing residuals to the intrinsic noise level of the instrument under heterogeneous field conditions, and to define a correction protocol that is transferable and compatible with applied microgravity workflows.

3.1 Materials

The measurements analysed in this chapter were acquired using Scintrex CG-5 Autograv relative gravimeters, portable spring-based instruments designed for high-resolution microgravity surveys, with a digital resolution of 1 μGal and typical field repeatability better than 5 μGal. Gravity readings are internally averaged over user-defined integration times after correction for tides, linear drift and tilt, providing time series suitable for monitoring subtle temporal variations at fixed locations. [9], [12], [15], [19].

Survey duration, spatial extent and acquisition redundancy directly control the temporal sampling of fixed reference points, the number of repeated measurements, and the capability to resolve systematic temporal effects in CG-5 records. Short surveys with limited base reoccupations primarily probe short-term instrument stability, whereas long-duration campaigns with dense base-station sampling enhance sensitivity to slow, non-linear temporal components. As illustrated by the range of operational settings shown in Figure 38, the analysed dataset spans markedly different mechanical, logistical and environmental conditions typical of applied microgravity surveys. The surveys summarised in Table 17 and Table 18 therefore provide a consistent and internally comparable framework for analysing time-dependent instrumental behaviour under realistic field conditions, while avoiding site-specific tuning of the correction strategy.

Table 17. Overview of surveyed sites, including site environment and primary survey target.

ID	Site	Site environment	Target
1	Brica di Sillano (Lucca, Italy)	Mountainous	Cavities detection
2	Pigneto (Rome, Italy)	Urban	Cavities detection
3	Tivoli [phase 1] (Rome, Italy)	Urban	Cavities detection
4	Tivoli [phase 2] (Rome, Italy)	Urban	Cavities detection
5	Fujairah (UAE)	Rock desert	Mineral exploration
6	Rio Marina (Elba Island, Italy)	Insular	Sinkhole detection
7	Tivoli (Rome, Italy)	Urban	Cavities detection
8	Colle Mentuccia (Rome, Italy)	Urban	Infrastructure modelling
9	San Giovanni (Arezzo, Italy)	Laboratory	Drift characterization

Table 18. Key characteristics of gravity surveys conducted between 2020 and 2025. Columns report survey duration (h), number of repeated base-station occupations, total number of gravity stations, and survey area (m²), which are operational descriptors relevant to data quality and repeatability.

ID	Start date	End date	Duration [h]	Base station occupation	Gravity stations	Survey area [m²]
1	16/03/2021	31/03/2021	359	29	404	18000
2	22/03/2022	28/03/2022	134	23	400	6000
3	20/07/2022	29/08/2022	962	41	462	50000
4	15/02/2023	22/02/2023	183	14	788	50000
5	07/12/2023	25/03/2024	2608	87	1600	15000000
6	15/03/2025	27/03/2025	295	29	660	7500
7	08/04/2025	17/04/2025	224	37	680	4500
8	03/07/2025	31/07/2025	230	14	250	600
9	24/09/2025	15/10/2025	505	25069	/	/

Figure 38. Scintrex CG-5 gravimeter in different survey environments: (a) installation along a vegetated rural path, (b) data acquisition in a roadside urban setting, and (c) deployment on steep rocky terrain within a mountainous desert landscape.

3.2 Methods

The overall operational and processing workflow adopted in this study is summarised in Figure 39. The procedure comprises two main phases: field acquisition and data processing. The field phase includes repeated base-station occupations and controlled memory management, whereas the processing phase consists of memory-jump correction followed by a two-stage harmonic modelling (LF + HF) and statistical model selection.

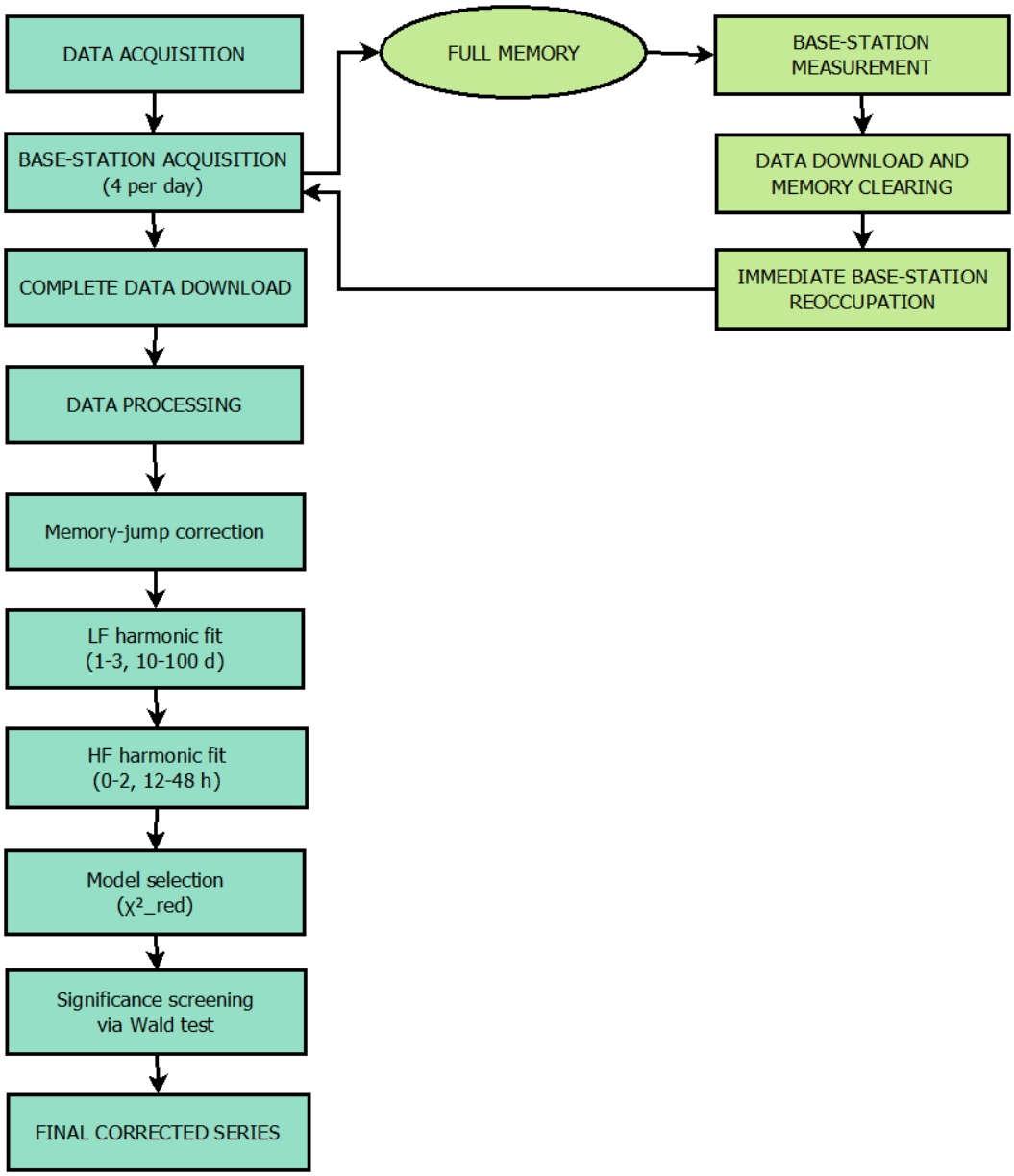

Figure 39. Operational and processing workflow adopted in this study. The field phase includes repeated base-station occupations, memory download and clearing, and immediate reoccupation after each reset to ensure temporal continuity. The processing phase comprises memory-jump correction, low-frequency (LF) harmonic modelling (1–3 harmonics, 10–100 days), high-frequency (HF) harmonic modelling (0–2 harmonics, 12–48 hours), model selection based on minimisation of the reduced weighted chi-square, and generation of the final corrected gravity series.

Within this framework, each survey included a dedicated reference base station used to monitor the temporal response of the gravimeter under nominally constant gravity. Base stations were established at locations meeting the minimum requirements of stability, isolation, accessibility and environmental control summarised in Table 19. In practice, benchmarks were installed on solid, levelled surfaces with well-constrained geodetic positioning, preferentially in sheltered settings and away from vibration sources and groundwater influences, in order to minimise external perturbations. During field operations, the base station was repeatedly reoccupied, typically two to four times per day, providing a time series of reference measurements used to characterise systematic temporal effects.

Table 19. Minimum requirements for the reference/base installation used for drift characterization. Aspects include stability, isolation, access/protection, positioning/marker, and environmental control [13], [14].

Aspect	Requirement
Stability	Solid, levelled surface on bedrock or reinforced concrete; located in a structurally stable area.
Isolation	Distant from vibration sources (> 0.5 Hz) and from groundwater or infiltration zones.
Accessibility/Protection	Easily reachable for frequent reoccupations; preferably sheltered or indoor (basement, ground floor).
Marker/Positioning	Permanent benchmark; geodetic coordinates known to < 1 m horizontally and < 0.3 m vertically.

Long-duration surveys required periodic clearing of the instrument memory, which introduces discontinuities in the recorded gravity series. Each memory reset partitions the base-station record into consecutive acquisition segments. To preserve temporal continuity, a standardised operational protocol was adopted: immediately before and after each memory clearing, the base station was reoccupied under unchanged environmental conditions. Given the negligible gravity variations at minute time scales, the last base measurement preceding the reset and the first measurement following the reset are assumed to sample the same gravity value.

In the processing workflow, memory resets are automatically detected as abrupt steps in the base-station time series exceeding a fixed threshold (5 mGal) between consecutive readings. For each detected reset, the gravity offset Δg is computed as the difference between the final base measurement of segment *i* and the initial base measurement of segment *i+1*. This offset is applied as a constant correction to all subsequent measurements within segment *i+1*, thereby stitching the segments into a single continuous reference series. This correction step is a prerequisite for any subsequent drift modelling, as it removes artificial offsets unrelated to instrumental drift or environmental forcing and ensures dynamic consistency across acquisition blocks (Figure 40).

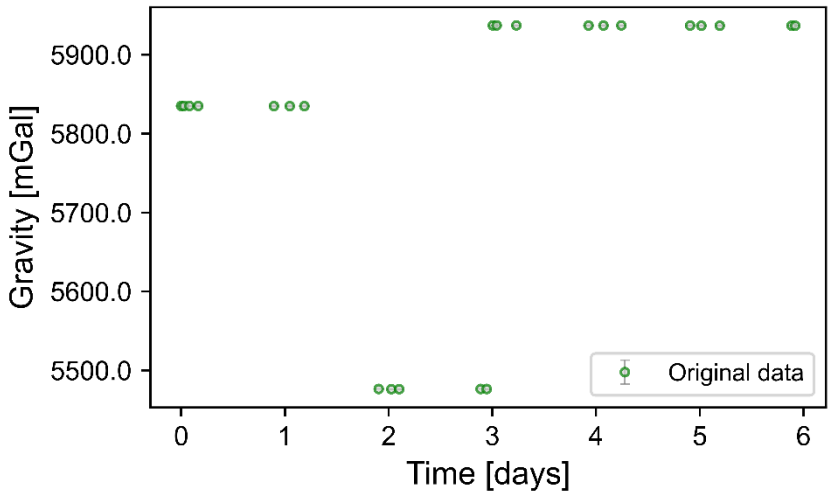

Figure 40. Example of memory-jump correction. After a memory wipe, the base station was immediately reoccupied; consecutive base readings define the offset Δg, which is applied as a constant correction to the subsequent acquisition segment to realign the time series into a single continuous reference curve.

After quality control based on the instrument standard deviation and after stitching memory related offsets, each dataset is represented by a single continuous base station time series $g_{\mathrm{mj}}(t_j)$, sampled at irregular times t_j. On the time scales considered here, gravity at a fixed benchmark is treated as constant within measurement uncertainty. Therefore, the observed temporal variability of $g_{\mathrm{mj}}(t)$is interpreted as the superposition of a deterministic instrumental component and a stochastic component consistent with the instrument noise and residual external disturbances.

3.2.1 Linear sine cosine parameterisation

The deterministic component is modelled as a sum of harmonic contributions plus a constant offset. Instead of fitting amplitudes and phases directly, the model is expressed in a sine cosine basis that is linear in the regression coefficients, which allows a closed form weighted least squares solution for any fixed set of angular frequencies. Specifically, for a set of Nangular frequencies $\{\omega_i\}_{i=1}^{N}$, the model is

$$m(t) = \sum_{i=1}^{N} [S_i \sin(\omega_i t) + c_i \cos(\omega_i t)] + B \quad (1)$$

where $s_i$and $c_i$are the linear coefficients, and $B$is a constant offset. Amplitude and phase are recovered a posteriori through

$$A_i = \sqrt{s_i^2 + c_i^2}\ ;\ \phi_i = arctan2(c_i, s_i) \quad (2)$$

so that each term is equivalently $A_i \sin(\omega_i t + \phi_i)$. This formulation follows standard multi sine fitting practice and provides a transparent separation between the nonlinear part of the problem, namely frequency selection, and the linear estimation of coefficients once frequencies are fixed [37], [38].

3.2.2 Weighted least squares solution and covariance

Each base reading $g_{\mathrm{mj}}(t_j)$is associated with the CG5 internal standard deviation σ_j, which is computed by the instrument from the scatter of the underlying samples contributing to the integrated reading, after internal filtering and spike rejection, and reported in the output file as SD or sigma [9]. These values quantify the within reading variability and are used as heteroscedastic uncertainties in weighted least squares, with weights $w_j = 1/\sigma_j^2$.

Let g be the vector of observations, and X the design matrix whose columns are $\sin(\omega_i t_j)$, $\cos(\omega_i t_j)$, and a column of ones for the offset. The model reads

$$g = \mathrm{X}\beta + \varepsilon \tag{3}$$

where βcollects all s_i, $c_i$and B. Minimising the weighted sum of squared residuals

$$S(\beta) = \sum_{j=1}^{n} \left(\frac{g_j - (\mathrm{X}\beta)_j}{\sigma_j}\right)^2 \tag{4}$$

leads to the normal equations $\mathrm{X}^T\mathrm{W}\mathrm{X}\,\hat{\beta} = \mathrm{X}^T\mathrm{W}\mathrm{g}$, with $\mathrm{W} = \mathrm{diag}(1/\sigma_j^2)$, and hence to the weighted least squares solution

$$\hat{\beta} = (\mathrm{X}^T\mathrm{W}\mathrm{X})^{-1}\mathrm{X}^T\mathrm{W}\mathrm{g} \tag{5}$$

The residual vector is $\mathrm{r} = \mathrm{g} - \hat{\mathrm{g}}$. The reduced chi square is computed as

$$\mathrm{X}^2_{red} = \frac{1}{v}\sum_{j=1}^{n}\left(\frac{r_j}{\sigma_j}\right), \qquad v = n - p \tag{6}$$

where p is the number of fitted parameters. For the multi harmonic model, $p = 2N + 1$. The parameter covariance matrix is estimated as

$$cov(\hat{\beta}) = \mathrm{X}^2_{red}(X^T W X)^{-1} \tag{7}$$

which propagates both the weighting and the observed residual variance.

3.2.3 Frequency selection and optimisation strategy

The core nonlinear problem is the selection of the angular frequencies ω_i. The workflow implements a deterministic grid-based coordinate descent scheme combined with a multi start strategy to reduce dependence on initialisation. Suggested methodological references for coordinate descent include [39].

3.2.4 Low frequency stage

The low frequency component is intended to capture slow instrumental drift over multi day scales. The search space is defined in terms of period bounds $T \in [10,100]$ d, discretised into a dense grid and mapped to angular frequencies through $\omega = 2\pi/T$. Candidate models with $N_{LF} \in \{1,2,3\}$ harmonics are evaluated.

For each N_{LF}, a set of random initial frequency vectors is drawn uniformly over the global search band. For each initialisation, frequencies are refined by coordinate descent: each $\omega_k$is updated by scanning the full grid while keeping the other frequencies fixed, and selecting the value that minimises χ^2_{red}under the constraints defined below. The algorithm cycles over all harmonics for a fixed maximum number of iterations or until the improvement in χ^2_{red} becomes negligible. A minimum separation in period is enforced, with $\Delta T_{min} = 10$ d, to reduce degeneracy between near identical harmonics.

3.2.5 High frequency stage

After the low frequency fit, the residuals

$$r_{LF}(t_j) = g_{mj}(t_j) - m_{LF}(t_j) \tag{8}$$

are optionally modelled by a high frequency harmonic component intended to capture sub daily periodicities. The high frequency search is constrained to $T \in [12,48]$ hand considers $N_{HF} \in \{1,2\}$. The optimisation follows the same multi start plus coordinate descent strategy, enforcing a minimum separation $\Delta T_{min} = 2$ h.

3.2.6 Model selection

For each stage, the deterministic component is tested against a discrete set of candidate harmonic configurations, spanning the allowed model orders and period bounds. Each candidate is estimated by weighted least squares using the CG 5 SD as observational uncertainty, and its fit quality is quantified through the corresponding reduced weighted chi square computed as in equation (6). The adopted model for the stage is the feasible candidate that yields the minimum reduced weighted chi square among all tested configurations, subject to the feasibility constraints imposed on periods and amplitudes.

3.2.7 Significance screening via Wald test

After selecting the LF and HF models, the statistical significance of each harmonic is assessed with a Wald test on the pair of coefficients (s_i, c_i). For each harmonic, the null hypothesis is

$$H_0: s_i = 0\ c_i = 0 \tag{9}$$

and the Wald statistic is

$$W_i = b_i^T C_i^{-1} b_i \tag{10}$$

where $\mathrm{b}_i = [s_i, c_i]^T$ and C_i is the 2×2 covariance submatrix extracted from $\mathrm{cov}(\hat{\beta})$. Under H_0, W_i follows a chi square distribution with 2 degrees of freedom, and the p value is computed accordingly. Harmonics with p value greater or equal to 0.05 are flagged as not significant and removed, and the model is refitted using only the retained harmonics [40].

3.2.8 Corrected gravity series

The deterministic drift model is removed sequentially. After the LF fit, the intermediate residual series is r_{LF}as in equation (8). After the optional HF fit, the final residuals are

$$r_{final}(t_j) = r_{LF}(t_j) - m_{HF}(t_j) \tag{11}$$

and the corrected series can be expressed as

$$g_{corr}(t_j) = g_{mj}(t_j) - m_{LF}(t_j) - m_{HF}(t_j) \tag{12}$$

For the final residuals, the degrees of freedom are computed as

$$v_{final} = N - (2N_{LF} + 2N_{HF} + 1) \tag{13}$$

and $\chi^2_{red,final}$ is evaluated as in equation (6).

The primary amplitude metric for residuals is the weighted root mean square error

$$WRMSE = \sqrt{\frac{\sum_j \omega_j r_j^2}{\sum_j \omega_j}} \tag{14}$$

reported in microGal. Bias is summarised using three complementary estimators: the arithmetic mean of r_{final}, the median of r_{final}, and the weighted mean

$$\bar{r}_\omega = \frac{\sum_j \omega_j r_j}{\sum_j \omega_j} \tag{15}$$

3.2.9 Histogram bin selection

Residual histograms are included to visualise the distribution shape. The number of bins is selected automatically using the Freedman Diaconis rule when the interquartile range is non zero, with bin width

$$h = 2\, IQR N^{-1/3} \tag{16}$$

and bins approximately equal to the residual range divided by h. If $IQR = 0$, a Rice type rule is used as a fallback. The number of bins is finally constrained within 6 and 30 to guarantee readability and comparability across sites [41].

3.3 Results

Base-station records from the San Giovanni benchmark and the eight field campaigns exhibit pronounced temporal variability, even though true gravity at a fixed reference point can be regarded as constant over the survey interval. Rather than remaining within the nominal single-reading repeatability of the CG-5 (5 µGal), the series show smooth oscillations from hourly to multi-day scales, with peak-to-peak amplitudes reaching up to 3376 µGa (Table 20). This behaviour indicates that variance is dominated by structured low-frequency components rather than by random measurement scatter.

Figure 41 illustrates the San Giovanni base station sequence together with the composite LF+HF drift model, and the corresponding final residuals obtained after subtracting both components as in equation (1). In the left panel, the combined curve reproduces the slow multi day modulation as well as the superimposed shorter period oscillations over the 21-day interval. The upper right panel shows the histogram of the final residuals, with a Gaussian curve superimposed, while the lower panel reports the same residuals as a function of time, highlighting their stationarity after correction and allowing direct inspection of any remaining temporal structure. The residual distribution is approximately symmetric and centred close to zero, and its width is consistent with the standard deviation estimated from the time series. Residuals are therefore well approximated by a Gaussian with near zero mean, supporting the use of χ^2_νas a goodness of fit metric for the LF+HF model.

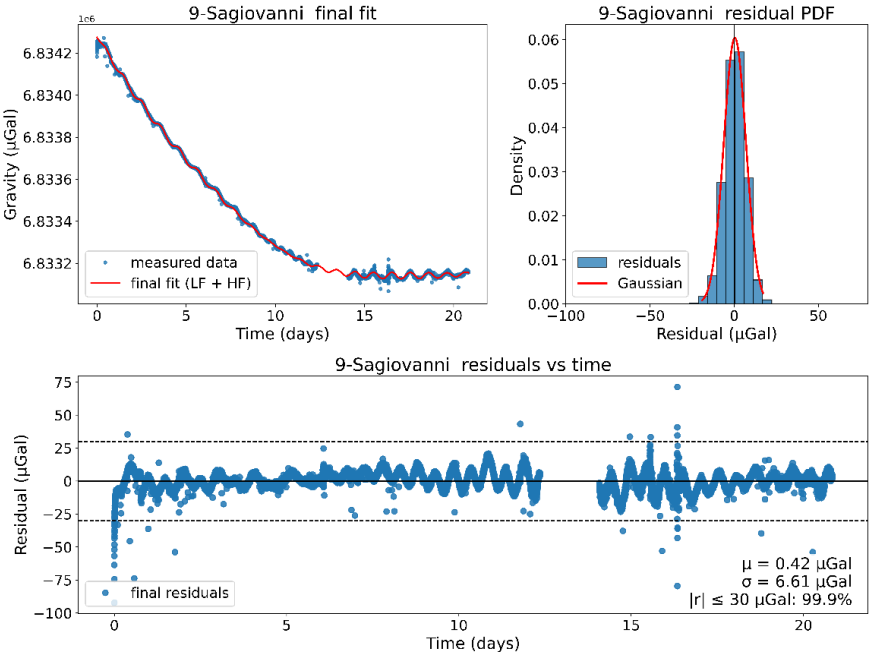

Figure 41. San Giovanni benchmark: final LF+HF fit (top left), Gaussian probability density of final residuals (top right), and residuals versus time with ±30 µGal reference band (bottom). Residuals are centred near zero (µ = 0.42 µGal, σ = 6.61 µGal), with 99.9% of values within ±30 µGal.

To quantify the variability at the base station before any deterministic correction, the mean and standard deviation of the gravity readings were computed for each dataset. Table 20 reports the number of base-station occupations, the mean base-station gravity (after standard processing corrections) in mGal and the corresponding standard deviation in μGal. Standard deviations range from about 77 μGal at Bagni di Tivoli to about 3370 μGal at Tivoli, consistently exceeding the nominal 5 μGal repeatability by one to two orders of magnitude. The raw base-station scatter is therefore dominated by systematic temporal components that must be modelled to achieve microgal-level internal consistency.

Table 20. Summary statistics of base-station gravity for all datasets n is the number of base-station occupations; mean corrected gravity g_{corr} is expressed in 10^3 μGal and standard deviation σ is in μGal.

Site	n	Meang_{corr} [10^3 μGal]	σ [μGal]
1	12	5638	407
2	29	5834	238
3	23	5986	3376
4	14	6131	77
5	101	4959	141
6	29	6732	744
7	37	6638	592
8	14	6687	703
9	25498	6833	348

The deterministic component of the base station sequences was modelled through a two-stage harmonic approach. After memory jump stitching, each series $g_{mj}(t_j)$ is first described by a low frequency component $m_{LF}(t)$, fitted as the sum of one to three harmonic terms whose periods are constrained within the 10-to-100-day band. This LF stage captures the slow, campaign scale drift like modulation that dominates the variance of the raw base station record and is commonly referred to in the geophysical literature as a low frequency contribution. The residuals of the LF fit, $r_{LF}(t_j)$ as defined in equation (**8**), are then analysed to identify and remove remaining systematic oscillations through a high frequency component $m_{HF}(t)$, defined in the 12 to 48 hour band and fitted with up to two harmonic terms. In practice, the HF step is introduced only to suppress structured sinusoidal patterns still visible in r_{LF}, thereby improving the stationarity of the final residuals without altering the slow trend already accounted for by m_{LF}.

The San Giovanni experiment provides a controlled reference dataset to illustrate the two-stage decomposition and to report representative parameters. In the first stage, the low frequency component $m_{LF}(t)$ is modelled using the harmonic WLS formulation introduced in eq. (1), with amplitudes and phases recovered from the sine cosine coefficients through eq. (2). The LF model order and its optimal set of angular frequencies are selected by minimising the reduced weighted chi square defined in eq.(**6**) among feasible candidates. Table 21 summarises the resulting LF parameter set in terms of N_{LF}, periods, amplitudes and phases, with one standard deviation uncertainties obtained from the period scanning procedure described in the Methods.

In the second stage, the LF residuals $r_{LF}(t_j)$ are defined as in eq.(**8**) and are used as input to an analogous harmonic WLS fit to obtain the high frequency component $m_{HF}(t)$, again adopting the model structure of eq. (1) and the coefficient to amplitude phase mapping of eq.(2). The HF order and frequencies are selected by the same reduced weighted chi square criterion of eq. (6). Table 22 reports the corresponding HF parameters, highlighting the sub daily periodic terms required to suppress the remaining deterministic structure in r_{LF}. The final corrected series is obtained by subtracting both contributions from the stitched observations, as in eq. (12). The goodness of fit is then evaluated on the final residuals $r_{final}(t_j)$ using the reduced weighted chi square of eq. (6) with degrees of freedom defined in eq. (13), and is reported in the statistical summary table in the next subsection.

Table 21. San Giovanni LF fit parameters $m_{LF}(t)$ from WLS. For each LF harmonic: A(μGal), $\omega(rad\ s^{-1})$, T(days), ϕ(rad) with 1σ uncertainties from the frequency scan LF order selected by minimum $\chi^2_{\nu,\mathrm{WLS}}$.

A [μGal]	ω [rad s-1]	T [d]	f [rad]
22 ± 0	$5.9 * 10^{-6}$	12	−1.23 ± 0.01
11174 ± 14	$1.9 * 10^{-6}$	39	−1.08 ± 0.02
2209 ± 26	$1.5 * 10^{-6}$	49	2.58 ± 0.01

Table 22. San Giovanni HF fit parameters $m_{HF}(t)$ from WLS on LF residuals $r_{LF}(t_j)$(eq. 8). For each HF harmonic: A(μGal), $\omega(rad\ s^{-1})$, T(hours), ϕ(rad) with 1σ uncertainties from the frequency scan. HF order selected by minimum $\chi^2_{\nu,\mathrm{WLS}}$.

A [μGal]	ω [rad s-1]	T [h]	f [rad]
7 ± 0.05	$6.7 * 10^{-5}$	25.89 ± 0.03	−0.48 ± 0.01
8 ± 0.05	$7.3 * 10^{-5}$	23.89 ± 0.02	−2.30 ± 0.01

The San Giovanni experiment provides a controlled benchmark to validate the full two stage LF plus HF decomposition. The statistical diagnostics computed on the final residuals $r_{final}(t_j)$ after applying the combined correction of equation (12) are summarised in Table 23.

Table 23. San Giovanni final residual statistics after the combined LF plus HF correction: number of readings N, selected LF order N_{LF}, reduced weighted chi square χ^2_ν, WRMSE, residual mean μ and standard deviation σ (all in µGal).

Site ID	N	N_{LF}	N_{HF}	X^2_{LF}	$WRMSE_{LF}$ [µGal]	µ [µGal]	σ [µGal]
9	25000	3	2	0.02	5.27	0.42	6.61

The San Giovanni results show residuals centred close to zero and a dispersion consistent with the expected measurement noise level, indicating that the deterministic structure is effectively removed without introducing spurious artefacts. On this basis, the same two stage workflow was applied unchanged to the eight-field base station time series. For each site, the stitched sequence $g_{mj}(t_j)$ was decomposed into a low frequency component $m_{LF}(t)$capturing the slow instrumental drift and long period modulation, and a high frequency component $m_{HF}(t)$aimed at removing the residual sinusoidal structure still visible after the LF correction.

In the LF stage, $m_{LF}(t)$was estimated on $g_{mj}(t_j)$using the constrained harmonic parameterisation introduced in the Methods. The preferred LF model order was selected among feasible candidates by minimising the reduced weighted chi square, χ^2_ν, as defined in equation (6). The Wald test was used as an additional safeguard to prevent unnecessary increases in complexity when the improvement was not statistically supported. A compact summary of the LF selection, including the selected $N_{LF}$and the associated goodness of fit metrics, is reported for all eight sites in Table 24, while the complete set of LF parameters is provided in Appendix, Table A 1.

Table 24. Low frequency fit statistics for the eight field sites: number of readings N, selected LF harmonic order N_{LF}, reduced weighted chi square $\chi^2_{\nu,LF}$, and WRMSE of the LF residuals (µGal).

Site ID	N	N_{LF}	X^2_{LF}	$WRMSE_{LF}$[µGal]
1	29	2	1.29	12.5
2	23	2	2.31	54.3
3	41	2	4.10	52.0
4	14	1	0.84	41.3
5	87	3	5.89	30.5
6	29	2	4.37	39.6
7	37	1	0.03	15.8
8	14	1	0.68	30.6

Figure 42 shows the resulting LF fits superimposed on the measured base station data for all field campaigns. Despite the diversity of survey durations and sampling patterns, the LF component reproduces the dominant slow variability and provides a stable baseline for the subsequent HF analysis.

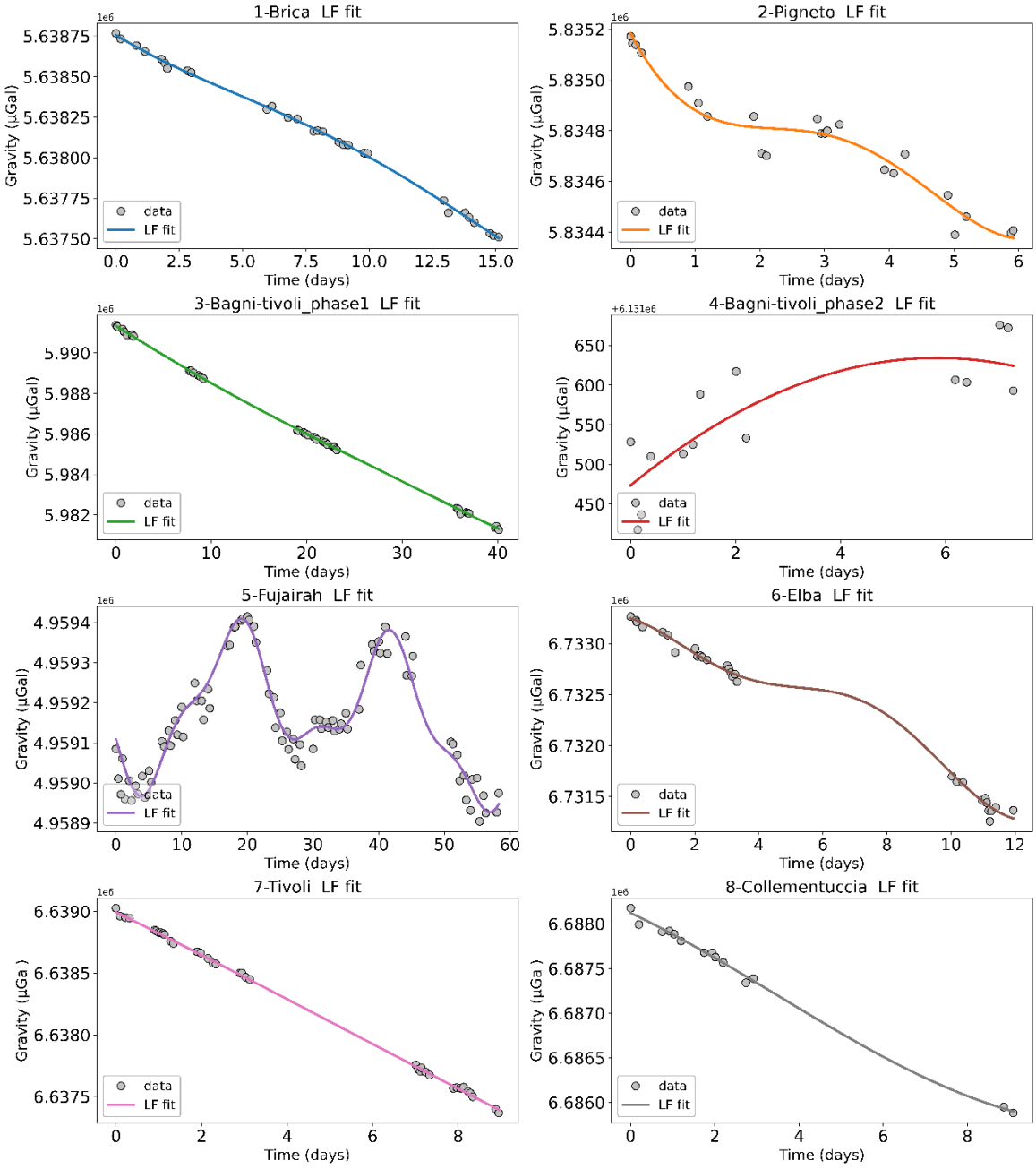

Figure 42. Low frequency fits for the eight field base stations. For each site, the stitched gravity series $g_{mj}(t_j)$is shown together with the selected LF model $m_{LF}(t)$, whose order is determined by minimisation of the reduced weighted chi square.

The HF stage was then performed on the LF residuals, defined in equation (8).

This step targets the deterministic oscillations that remain visible after the removal of the low-frequency component and that typically appear as quasi-sinusoidal structures on sub-daily time scales.

For each site, candidate HF models with increasing harmonic order were first estimated by weighted least squares, and the preferred order was selected by minimising the reduced weighted chi square defined in equation (6). As in the LF stage, the model selected on the basis of the minimum χ_ν^2 was then subjected to a Wald significance test on the harmonic coefficients. When one or more harmonics were found to be statistically non-significant, the model was refitted retaining only the significant terms, thereby preventing over-parameterisation while preserving the minimum-χ_ν^2 selection criterion.

The resulting HF summary for the eight field datasets is reported in Table 25, which lists, for each site, the selected number of HF harmonics N_{HF}, the corresponding reduced weighted chi square, and the WRMSE evaluated on the LF residuals. The complete set of HF parameters (amplitudes, angular frequencies, phases and offsets) is provided in Appendix A, Table A 2.

Table 25. High frequency fit statistics for the eight field sites: selected HF harmonic order N_{HF}, reduced weighted chi square $\chi^2_{\nu,HF}$, and WRMSE of the HF residuals (µGal).

Site ID	N_{HF}	X^2_{Final}	$WRMSE_{HF}$[µGal]
1	2	0.56	7.5
2	2	0.66	25.6
3	2	1.60	30.6
4	2	0.14	13.4
5	2	4.26	25.3
6	1	3.00	31.4
7	2	0.01	9.3
8	2	0.14	11.0

Figure 43 shows the HF fits superimposed on the LF residuals for all eight sites, illustrating how the sub-daily component suppresses the remaining structured oscillations.

The final corrected series is obtained by subtracting both LF and HF contributions, as expressed in equation (12).

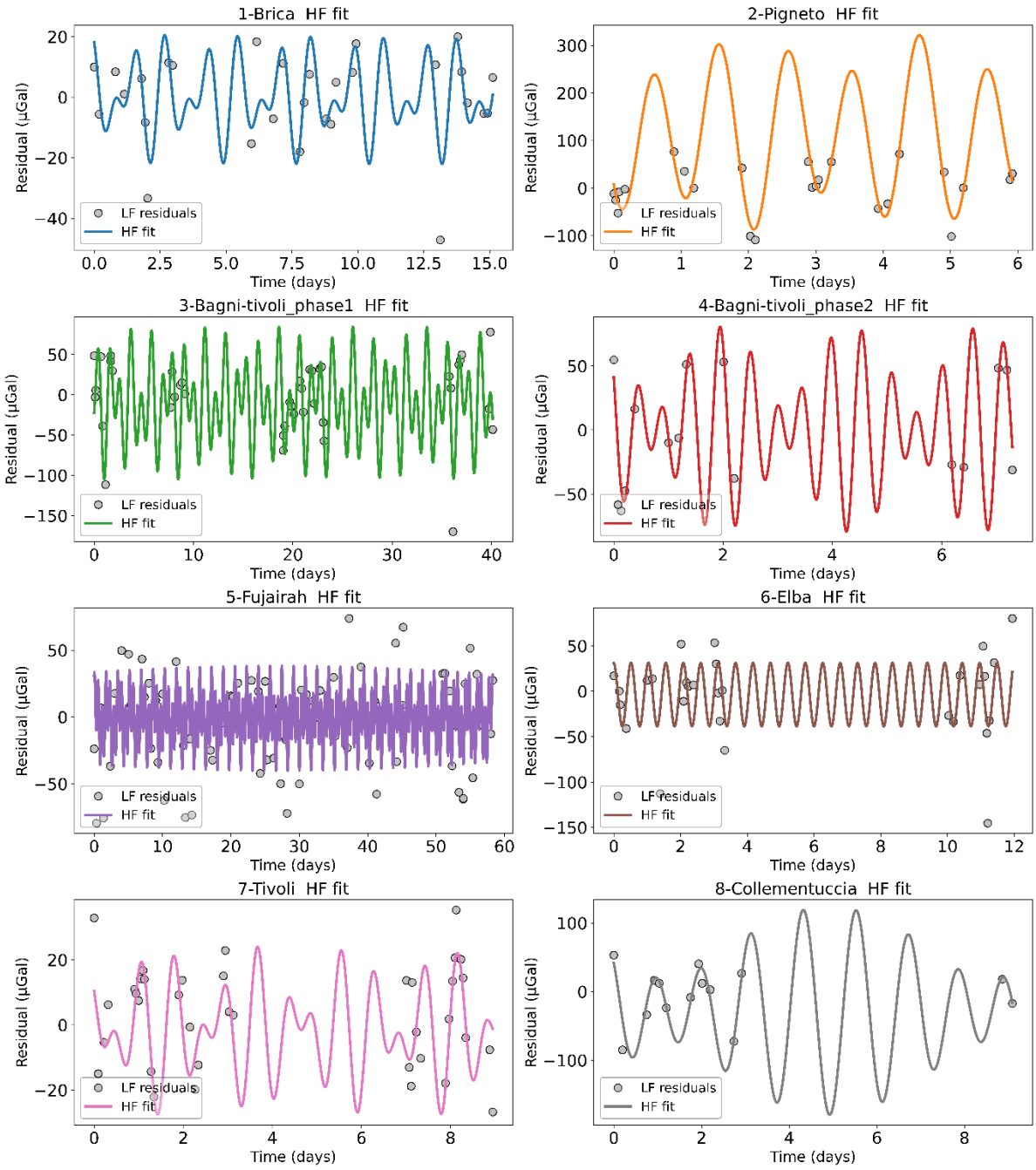

Figure 43. HF best fits superimposed on LF residuals for all field datasets. Points represent LF residuals; solid curves are the selected HF models obtained after χ^2 minimisation and Wald-test refit. Time is referenced to survey start (days); residuals are in μGal.

The statistical evaluation is then performed on the final residuals associated with equation (12). The reduced chi square reported in the batch summary as $\chi^2_{\nu,FINAL,}$ corresponds to equation (6) evaluated on the final residuals, with the degrees of freedom computed according to equation (13).

Before presenting the temporal behaviour of the corrected series, Table 26 summarises the statistical properties of the final residuals for all sites. In addition to the residual mean $\mu$and standard deviation σ, expressed in μGal, the table includes the percentage of data falling within the ±30 μGal band.

The ±30 μGal threshold is not arbitrary. It is motivated both by the available bibliographic [7], [42], [43] evidence on post-correction CG-5 base-station performance and by the controlled laboratory test conducted at San Giovanni. As shown in Figure 41 99.9% of the laboratory residuals fall within the ±30 μGal range after application of the full LF+HF correction. This interval is therefore adopted as a practical reference band representative of the expected residual noise level of the base station after systematic components have been removed.

The percentage of observations within ±30 μGal provides an immediate and physically interpretable performance indicator, complementary to σ. While the standard deviation measures dispersion assuming approximate symmetry, the ±30 μGal fraction directly quantifies how much of the corrected signal is consistent with the empirically validated noise envelope.

Table 26. Final residual statistics after LF+HF correction. For each site, mean μ, standard deviation σ (μGal), and percentage of residuals within the ±30 μGal reference band are reported.

Site ID	μ [μGal]	σ [μGal]	|r| ±30 [%]
1	-0.9	9.4	100%
2	-0.2	26.4	78%
3	0.7	32.8	70%
4	2.0	15.0	93%
5	-3.3	32.4	67%
6	-5.4	38.8	55%
7	0.8	11.0	100%
8	-3.6	14.8	93%

Figure 44 displays the final residuals versus time for all sites, together with the ±30 μGal reference band. This representation enables a direct assessment of residual stationarity, temporal independence and the absence of systematic drift after application of the two-stage LF+HF correction. The visual inspection confirms that, for all datasets, the residuals fluctuate around zero without coherent long-period trends, and that most observations remain confined within the expected post-correction noise envelope.

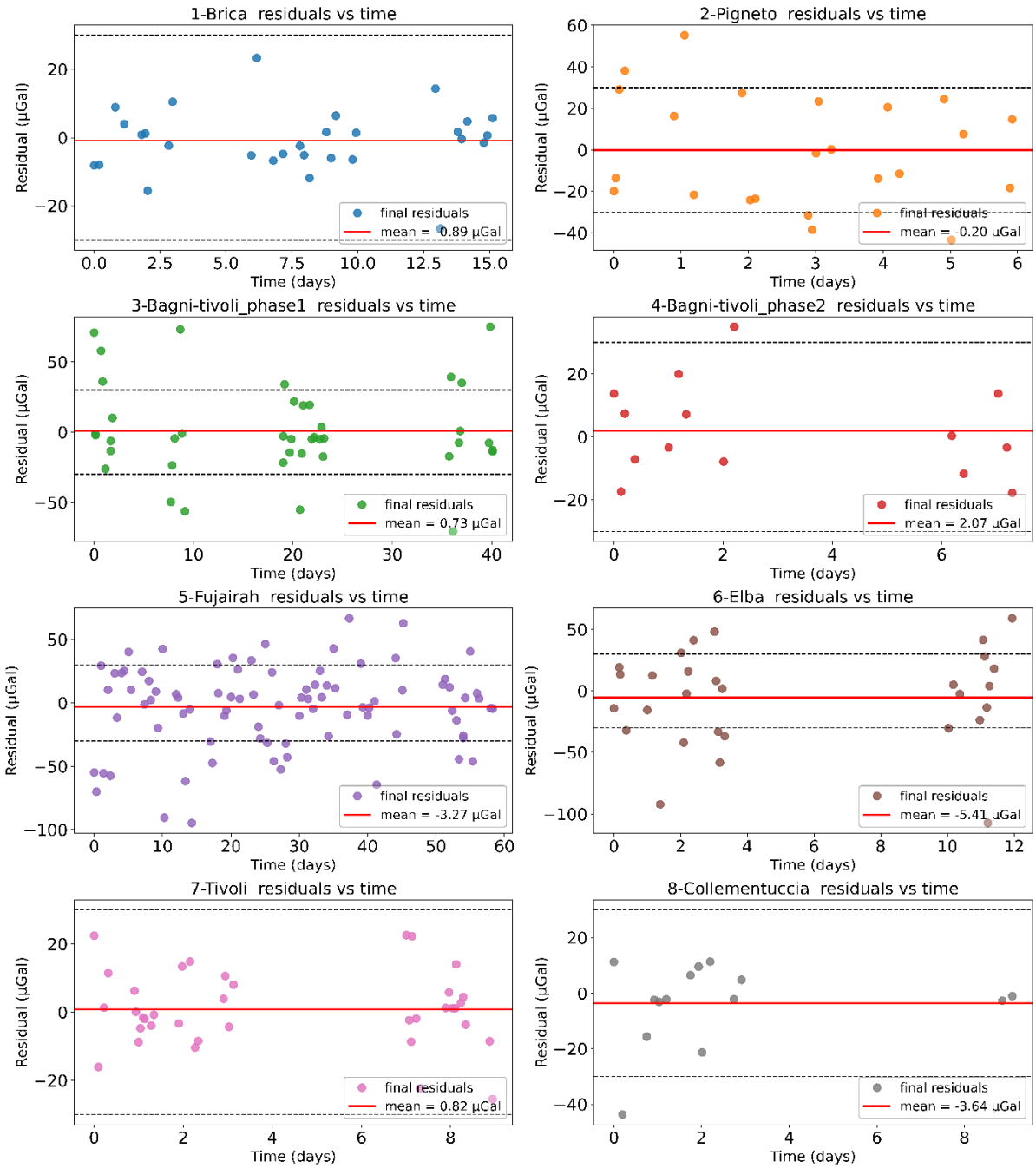

Figure 44. Final residuals versus time for the eight field datasets after LF+HF correction. Dashed lines indicate the ±30 µGal reference band; site-specific mean, standard deviation and percentage of points within the band are reported in each panel.

Overall, comparison between the pre-correction scatter metrics (Table 20) and the post-correction statistics reported in Table 25 and Table 26 demonstrates that the LF+HF workflow consistently reduces base-station variability across all field datasets. In most cases, the majority of residuals fall within the empirically defined ±30 µGal band, indicating that the corrected dispersion approaches the noise regime validated under controlled laboratory conditions, while preserving a uniform and reproducible processing strategy across heterogeneous survey environments.

3.4 Discussion

Residuals after onboard correction do not behave as pure random scatter, but exhibit structured variability on multiple time scales. In the controlled San Giovanni record, where sampling is dense and operating conditions are stable, the two-stage decomposition resolves this structure into a slow component captured by the LF model and a sub daily component captured by the HF model. In particular, the HF terms selected for San Giovanni cluster in the near diurnal band and match the principal diurnal tidal constituents: the fitted periods around 23.9 h and 25.8 h coincide with K1 and O1, respectively. This correspondence is physically meaningful because K1 and O1 dominate the diurnal solid Earth tide and associated loading contributions, so their appearance in the residual structure is consistent with tidal forcing modulating the gravimeter response under otherwise constant gravity [18], [44], [45]. When the same workflow is transferred to the eight field datasets, the HF periodicities remain within the prescribed 12 to 48 h band, but their estimated values should be interpreted as effective parameters. Sparse reoccupation schedules and irregular sampling reduce spectral resolution and can shift the optimum within the admissible band without implying a change in the underlying forcing. Their recurrence across contrasting environmental and operational contexts supports the use of a purely harmonic framework for modelling temporal bias [15].

Unlike polynomial or hybrid schemes, the adopted correction removes no secular trend and treats drift as a purely periodic signal estimated in two successive steps: LF on the stitched base record, followed by HF on the LF residuals. For each step, only a small set of feasible harmonic configurations is considered and the retained solution is required to provide a statistically defensible improvement, so that added terms reduce structured residuals without sacrificing interpretability [15], [20].

Model adequacy is supported by the final residual behaviour in both summary statistics and time domain diagnostics. Residual means in. Table 26 remain close to zero, while the dispersions are site dependent but compatible with the expected field scatter of CG 5 acquisitions. Consistently, the residuals versus time (Figure 44) show no persistent temporal structure after correction, and a large fraction of points falls within the ±30 μGal band, which is anchored to the San Giovanni benchmark and to literature noise levels [46] [47].

Gaussian probability density functions derived from the residual moments offer a compact cross site comparison of bias removal. The curves remain centred within a few μGal of zero, indicating that the workflow suppresses systematic offsets without introducing site specific bias.

Differences across sites are expressed mainly as changes in width, which is consistent with variable operational conditions such as transport, handling, micro vibrations, and environmental coupling, rather than with a remaining deterministic drift component.

The overall similarity of residual centering across sites, together with the absence of structured residual patterns in the time series, supports the operational transferability of the workflow and confirms that LF accounts for most of the variance while HF acts primarily as a targeted cleanup of the remaining sinusoidal structure.

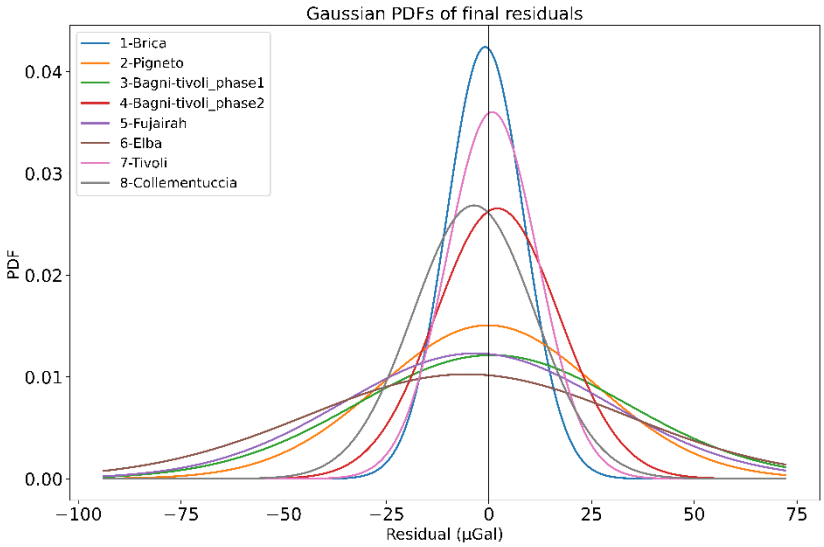

Figure 45. Probability density functions of base-station residuals for all sites. Curves show the estimated Gaussian probability density functions of the residuals after four-harmonic correction, expressed in mGal. Distributions are centred near zero (μ ≈ 0) with similar spread across environments, consistent with unbiased residuals and homogeneous noise levels.

Previous investigations of CG-5 behaviour have documented both short- and long-term drift trends [7], [12], [15], [17], [19]. However, no standardised, widely adopted correction framework has been proposed for operational field use. Most approaches rely on high-order polynomial regressions or external calibration against absolute or superconducting gravimeters [15], [19], [48], [49], but these methods, while accurate, are impractical in geophysical surveys with industrial or operational objectives, where simple and reproducible procedures are required. his study addresses that methodological gap by delivering a standardised, fully reproducible industrial workflow that links operational acquisition practice to a physically constrained two stage drift correction within a single pipeline. As summarised in Figure 39, CG-5 campaigns are organised around a dedicated base station that is reoccupied several times per day, including an immediate pre and post reoccupation whenever the instrument memory is cleared.

This operational rule makes memory events observable as discrete steps and enables automatic stitching of acquisition segments through memory jump correction, producing a single continuous base station series suitable for modelling.

Drift is treated as the sum of two deterministic components estimated sequentially on the stitched base record. A low frequency harmonic stage captures the dominant slow instrumental drift and long period modulation, and a subsequent high frequency stage is applied to the LF residuals to remove the remaining sub daily sinusoidal structure. For each stage, a limited set of feasible harmonic configurations is compared and the preferred solution is retained only when the additional terms yield a statistically meaningful improvement; coefficients are then recomputed on the selected configuration to produce the final LF and HF parameter sets. The resulting correction delivers drift corrected gravity values ready for the usual spatial processing.

The key practical outcome is that drift handling no longer relies on case-by-case empirical choices or ad hoc polynomial terms. Instead, it becomes a repeatable and auditable procedure that can be applied unchanged across heterogeneous industrial settings, improving comparability between campaigns and providing a consistent accuracy benchmark for operational microgravimetry.

Across the analysed datasets, the workflow yields final residual standard deviations of 9–38 μGal, i.e. an improvement exceeding one order of magnitude relative to the instrument's onboard linear compensation. This residual dispersion is well below the gravity anomaly amplitudes typically targeted in applied microgravity (Table 27), which commonly span from a few tens to several hundreds of μGal depending on the application. As a consequence, the corrected data retain sufficient resolving power for confident interpretation of subsurface signals even when additional uncertainty sources associated with subsequent reductions are considered.

Residual diagnostics further support model adequacy. The final residual time series (Figure 44) show no systematic temporal structure and remain centred close to zero across sites, with mean values between −5.4 and +2.0 μGal. The Gaussian probability density functions (Figure 45), derived from the residual moments, are approximately symmetric around zero and exhibit site dependent but comparable widths, consistent with the σ values reported in Table 26.

The overall similarity of residual centering and dispersion across the different operational environments indicates that, after correction, the remaining variability is primarily controlled by measurement scatter and by site dependent external disturbances such as handling, logistics, micro vibrations, and variable environmental coupling, rather than by a persistent deterministic bias. Across all campaigns, the two stage LF plus HF decomposition behaves consistently, with the LF component capturing the dominant share of the slow drift and long period modulation, and the HF component providing a targeted removal of the residual quasi-sinusoidal structure that can remain visible after LF correction.

From an applied perspective, this defines a standardised industrial workflow for CG 5 base station processing that is reproducible and directly deployable. Candidate models are screened and ranked using the reduced weighted misfit, then the statistical relevance of the retained harmonic terms is checked with a joint significance test, and the final coefficients are recomputed on the selected set to prevent unnecessary complexity.

Table 27. Expected gravity anomaly ranges (µGal) for representative applied microgravity targets, compiled from literature sources [8], [20], [50], [51], [52], [53], [54], [55], [56], [57]. Reported values indicate typical anomaly amplitudes associated with mass deficits or redistributions in different settings. The table provides a reference scale to assess whether post correction residuals are sufficiently small for reliable interpretation.

Domain	Anomaly range (µGal)	Targets
Sinkhole	–30 to –50	Metric-scale sinkholes (2–5 m radius)
Urban Subsurface Investigations	–50 to –100	Anthropogenic and natural voids beneath built-up areas
Geotechnical Surveys	~20	Slope stability and infrastructure assessments
Mineral Exploration	~1000	Large-scale ore bodies (e.g., dense iron or massive sulfide deposits)
Volcanic Monitoring	–145 to +100	Mass changes in shallow magma reservoirs
Environmental Monitoring	+10 to +50	Landfill and contamination sites, subsurface mass redistributions
Archaeological Prospection	+20 to +200	Buried structures and archaeological features
Seismic/Geothermal Monitoring	+5 to +150	Real-time mass movements in geothermal fields and active fault zones
UXO Detection	+10 to +50	Detection of buried metallic objects (unexploded ordnance)
Industrial Structural Monitoring	+5 to +20	Machinery, plant, and civil infrastructure health (e.g., wind turbines)

The correction framework was intentionally limited to periods shorter than about two months, because extending the search to longer periodicities would provide little practical advantage for industrial and environmental campaigns, which typically last from a few days to a few weeks. Within this operational window, the two-stage model spans the frequency content that most strongly controls the observed base station variability, with the LF component capturing multi day to multi week modulation and the HF component accounting for residual sub daily oscillations that may persist after LF removal. For the longest LF terms, estimates become progressively less constrained as the record length approaches or falls below the corresponding period. In campaigns shorter than roughly two weeks, the slowest components should therefore be interpreted as effective parameters that absorb the low frequency curvature present within the available window rather than as uniquely resolved periodicities. This limited identifiability does not compromise the correction itself, because the reduction in base station scatter is driven mainly by the better constrained shorter LF content and by the HF cleanup on the LF residuals, which together dominate the variance reduction over typical acquisition durations.

4 Conclusion

Long CG-5 base station records acquired during one controlled benchmark test and eight operational microgravity campaigns were analysed to quantify the systematic temporal variability that biases field measurements if left uncorrected. Because gravity at a fixed benchmark can be treated as constant over the time windows considered here, the observed variability is interpreted as a gravimeter response driven by a deterministic component, potentially modulated by repeatable external forcing, plus a stochastic component associated with measurement scatter and residual environmental noise. In addition, long duration surveys required periodic memory clearing, which produces artificial offsets that must be removed by stitching consecutive acquisition segments before any drift modelling.

A standardised two stage harmonic workflow was therefore developed and applied to every stitched sequence. A low frequency component captures slow drift and long period modulation using one to three harmonic terms constrained to periods between 10 and 100 days. The LF residuals are then inspected for remaining structured oscillations and, where required, a high frequency component is estimated using zero to two harmonic terms constrained to periods between 12 and 48 hours. Both stages are solved by weighted least squares using the CG 5 internal SD as heteroscedastic uncertainty, and candidate model orders are ranked by their reduced weighted chi square, selecting the smallest feasible value, then controlled through a Wald test and final refit to obtain the definitive parameter set. The combined correction is applied as in equation (12), yielding drift corrected values that can be propagated directly to the spatial reductions.

The San Giovanni benchmark provides a controlled reference to validate the full processing chain. After LF plus HF correction, the HF periods are consistent with the diurnal tidal constituents K1 (23.9 h) and O1 (25.8 h), indicating that, under stable conditions and dense sampling, the remaining deterministic structure after LF is dominated by physically plausible diurnal forcing rather than by arbitrary instrumental instability. The final WRMSE of 5.7 μGal matches the repeatability stated in the CG-5 documentation, demonstrating that the workflow can reduce a long base station sequence to the instrumental noise floor when environmental coupling and handling are minimised. Consistently, nearly all corrected San Giovanni residuals fall within a ±30 μGal band, providing an operational reference threshold for post correction variability.

Application of the unchanged workflow to the eight field campaigns confirms transferability across heterogeneous conditions. In operational surveys, the residual dispersion is inevitably larger than in the laboratory benchmark, reflecting additional noise sources such as transport and handling, site dependent coupling, micro vibrations, variable thermal and mechanical environments, and irregular sampling. Nevertheless, residual means remain close to zero and residual dispersions remain within the target ranges required for applied microgravimetry, with a high fraction of points contained within the ±30 μGal reference band. Time domain inspection of the final residuals shows no systematic post correction temporal structure, supporting the conclusion that LF accounts for the dominant variance while HF acts primarily as a targeted removal of the residual sinusoidal component that survives LF correction.

Overall, this study defines a reproducible and operational protocol for CG-5 drift correction that combines base-station management, memory-jump handling, and harmonic modelling within a coherent processing framework. The procedure is fully specified in terms of selection criteria, optimisation strategy, and statistical tests, so that it can be applied by different operators without subjective tuning. Given the same input data and settings, the workflow yields consistent results, which supports transparent replication across surveys.

The correction scheme does not depend on site-specific empirical adjustments and was verified under different environmental and logistical conditions. For this reason, it can be implemented in heterogeneous field contexts without modifying the structure of the model. The drift-corrected gravity values can then be directly integrated into standard spatial processing steps, without the need for additional ad hoc temporal corrections.

The reproducibility of the proposed framework will be further assessed by applying the same correction strategy to datasets acquired with different relative gravimeter models, in order to evaluate its robustness beyond the CG-5 instrument and to analyse possible instrument-dependent drift behaviour.

.

Acknowledgments

We thank GeoExplorer for granting permission to use the CG-5 survey data for research purposes and for logistical support during field operations. We also thank Prof. Fabio Mantovani for his guidance and all those who contributed, even briefly, to the development of this thesis. Finally, we acknowledge the field crews involved in data acquisition and the reviewers for their constructive comments, which helped improve the clarity of this work.

Appendix A

Appendix A reports the complete harmonic parameter set obtained for all analysed datasets after model selection, Wald testing, and final weighted least squares refitting. The low frequency components are summarised in Table A 1, while the high frequency components and associated residual statistics are reported in Table A 2. For each site and for both LF and HF stages, all retained harmonic terms are listed together with their amplitudes, angular frequencies, periods, phases, offsets, and reduced chi square values.

Uncertainties correspond to one standard deviation. For both LF and HF components, amplitude, phase, and offset uncertainties are derived from the covariance matrix of the linear WLS solution, whereas angular frequency uncertainties are obtained from profile analysis using the $\Delta\chi^2 = 1$ criterion. When the $\chi^2(\omega)$ profile does not allow a bounded confidence interval within the admissible search range, the corresponding frequency uncertainty, and the propagated period uncertainty, are reported as not estimable.

Table A 1. Low frequency harmonic parameters for all datasets after model selection and Wald filtering. For each retained harmonic term the amplitude A, angular frequency ω, period T, phase φ, offset B, and reduced chi square χ^2_{red} are reported together with their one standard deviation uncertainties. Frequency uncertainties are derived from the $\Delta\chi^2 = 1$ profile criterion.

	1	2	3	4	5	6	7	8
A1 [µGal]	2030± 962	3676± 1312	44135± 1913	1214± 927	47± 5	350± 34	2892± 26	1476± 41
A2 [µGal	5952± 3008	1187± 395	37999± 1810	/	145± 5	830± 14	/	/
A3 [µGal]	/	/	/	/	111± 8	/	/	/
T1 [d]	46	20	100	70	10	10	100	32
T2 [d]]	84	10	94	/	24	20	/	/
T3 [d]	/	/	/	/	100	/	/	/
ω1 [rad/h]	0.0057	0.0131	0.0026	0.0037	0.0240	0.0262	0.00262	0.0081
ω2 [rad/h]	0.0031	0.0262	0.0028	/	0.0106	0.0131	/	/
ω3 [rad/h]	/	/	/	/	0.00262	/	/	/
f_1 [rad]	0.13± 0.20	-2.77± 0.11	1.98± 0.17	1.05± 0.15	2.75± 0.12	2.76± 0.20	2.77± 0.09	2.47± 0.07
f_2 [rad]	-2.56± 0.22	-0.65 ±0.15	-1.24± 0.18	/	-2.93± 0.04	1.14± 0.06	/	/
f_3 [rad]	/	/	/	/	-0.06± 0.05	/	/	/
B [µGal]	5641751 ± 2246	5837211 ± 959	5986850 ± 753	6130419 ±910	4959128 ± 6	6732362 ± 68	6637963 ± 277	6687207 ± 89

Table A 2. High frequency harmonic parameters and derived residual statistics for all datasets. Parameters are obtained from weighted least squares refitting after Wald selection. Angular frequency uncertainties are reported only when the $\Delta\chi^2 = 1$ profile yields a bounded interval.

	1	**2**	**3**	**4**	**5**	**6**	**7**	**8**
A1 [μGal]	10.28 ± 2.23	162.16 ± 26.70	53.73 ± 7.93	46.79 ± 7.44	15.36 ± 4.11	34.89 ± 9.37	13.29 ± 2.38	97.91 ± 15.12
A2 [μGa]	12.06 ± 2.25	42.42 ± 9.63	41.05 ± 8.61	33.33 ± 6.91	23.86 ± 4.32	/	12.59 ± 2.87	53.51 ± 11.89
T1 [h]	22.09 ± 0.23	23.67 ± 0.22	25.56 ± 0.04	12.36 ± 0.15	40.79 ± 0.11	12.54 ± 0.05	21.78 ± 0.00	27.45 ± 0.45
T2 [h]]	33.27 ± 0.44	38.45 ± 1.38	44.49 ± 0.18	15.78 ± 0.49	13.71 ± 0.01	/	15.29 ± 0.00	32.59 ± 1.18
ω1 [rad/h]	0.28 ± 0.003	0.26 ± 0.002	0.24 ± 0.0003	0.51 ± 0.006	0.15 ± 0.0004	0.50 ± 0.002	0.29 ± 0.000	0.23 ± 0.004
ω2 [rad/h]	0.19 ± 0.002	0.16 ± 0.005	0.14 ± 0.0005	0.40 ± 0.012	0.46 ± 0.0001	/	0.41 ± 0.0001	0.19 ± 0.007
f_1 [rad]	2.53 ± 0.22	-2.23 ± 0.06	-1.26 ± 0.15	2.95 ± 0.16	0.64 ± 0.25	1.65 ± 0.26	1.19 ± 0.19	2.79 ± 0.10
f_2 [rad]	1.52 ± 0.18	2.66 ± 0.19	1.27 ± 0.16	1.85 ± 0.23	1.26 ± 0.16	/	-3.13± 0.17	0.76 ± 0.19
B [μGal]	0.19 ± 1.57	116.74 ± 20.26	-10.41 ± 6.40	0.42 ± 4.55	-0.99 ± 2.82	-3.71 ± 6.31	-1.79 ± 1.75	-28.08 ± 5.49

Bibliography

[1] W. A. Heiskanen and H. Moritz, 'Physical geodesy', *Bulletin Géodésique (1946-1975)*, vol. 86, no. 1, pp. 491–492, 1967.

[2] X. Li and H.-J. Götze, 'Ellipsoid, geoid, gravity, geodesy, and geophysics', *Geophysics*, vol. 66, no. 6, pp. 1660–1668, 2001.

[3] W. J. Hinze, R. Von Frese, and A. H. Saad, *Gravity and magnetic exploration: Principles, practices, and applications*. Cambridge University Press, 2013.

[4] H. O. Seigel, I. Brcic, and P. Mistry, 'A guide to high precision land gravimeter surveys', *Scintrex Limited*, vol. 222, no. 1, pp. 1–122, 1995.

[5] N. Debeglia and F. Dupont, 'Some critical factors for engineering and environmental microgravity investigations', *Journal of Applied Geophysics*, vol. 50, no. 4, pp. 435–454, 2002.

[6] G. Tuckwell, T. Grossey, S. Owen, and P. Stearns, 'The use of microgravity to detect small distributed voids and low-density ground', *Quarterly Journal of Engineering Geology and Hydrogeology*, vol. 41, no. 3, pp. 371–380, 2008.

[7] S. Bonvalot, M. Diament, and G. Gabalda, 'Continuous gravity recording with Scintrex CG-3M meters: a promising tool for monitoring active zones', *Geophysical Journal International*, vol. 135, no. 2, pp. 470–494, 1998.

[8] D. Boddice, P. Atkins, A. Rodgers, N. Metje, Y. Goncharenko, and D. Chapman, 'A novel approach to reduce environmental noise in microgravity measurements using a Scintrex CG5', *Journal of Applied Geophysics*, vol. 152, pp. 221–235, 2018.

[9] C. Scintrex Limited, *CG-5 scintrex autograv system operation manual*. Scintrex Limited Concord, Ontario, 2006.

[10] M. Lederer, 'Accuracy of the relative gravity measurement', *Acta Geodyn. Geomater*, vol. 6, no. 3, p. 155, 2009.

[11] V. Dehant, P. Defraigne, and J. M. Wahr, 'Tides for a convective Earth', *Journal of Geophysical Research: Solid Earth*, vol. 104, no. B1, pp. 1035–1058, 1999.

[12] S. Onizawa, 'Apparent calibration shift of the Scintrex CG-5 gravimeter caused by reading-dependent scale factor and instrumental drift', *Journal of Geodesy*, vol. 93, no. 9, pp. 1335–1345, 2019.

[13] A. S. Murray and R. M. Tracey, 'Best practice in gravity surveying', *Geoscience Australia*, vol. 3, no. 5, 2001.

[14] J. R. Kennedy, D. R. Pool, and R. L. Carruth, 'Procedures for field data collection, processing, quality assurance and quality control, and archiving of relative-and absolute-gravity surveys', US Geological Survey, 2021.

[15] B. Elsaka, 'Comparison of different polynomial degrees for correcting the instrumental drift of Scintrex CG-5 Autograv gravimeter', *Australian Journal of Basic and Applied Sciences*, vol. 14, no. 5, pp. 19–25, 2020.

[16] R. Reudink *et al.*, 'High tilt susceptibility of the Scintrex CG-5 relative gravimeters', *Journal of Geodesy*, vol. 88, no. 6, pp. 617–622, 2014.

[17] H. Cheraghi *et al.*, 'Stability of the calibration of scintrex relative gravimeters as inferred from 12 years of measurements on a large amplitude calibration line in Iran', *Pure and Applied Geophysics*, vol. 177, no. 2, pp. 991–1004, 2020.

[18] I. M. Longman, 'Formulas for computing the tidal accelerations due to the moon and the sun', *Journal of Geophysical Research*, vol. 64, no. 12, pp. 2351–2355, 1959.

[19] B. Meurers, 'Scintrex CG5 used for superconducting gravimeter calibration', *Geodesy and Geodynamics*, vol. 9, no. 3, pp. 197–203, 2018.

[20] M. Battaglia, A. Calahorrano-Di Patre, and A. F. Flinders, 'gTOOLS, an open-source MATLAB program for processing high precision, relative gravity data for time-lapse gravity monitoring', *Computers & Geosciences*, vol. 160, p. 105028, 2022.

[21] P. Conti, G. Cornamusini, and L. Carmignani, 'An outline of the geology of the Northern Apennines (Italy), with geological map at 1: 250,000 scale', *Italian Journal of Geosciences*, vol. 139, no. 2, pp. 149–194, 2020.
[22] L. Carmignani, P. Conti, G. Cornamusini, and A. Pirro, 'Geological map of Tuscany (Italy)', *Journal of Maps*, vol. 9, no. 4, pp. 487–497, 2013.
[23] M. Menichini, M. Doveri, and L. Piccini, 'Hydrogeological and geochemical overview of the karst aquifers in the Apuan Alps (Northwestern Tuscany, Italy)', *Acque Sotterranee-Italian Journal of Groundwater*, vol. 5, no. 1, 2016.
[24] A. G. Leica Geosystems, *Leica Nova MS50 MultiStation*. Datasheet, 2013.
[25] F. Marra, F. Florindo, and C. Petronio, 'Quaternary fluvial terraces of the Tiber Valley: geochronologic and geometric constraints on the back-arc magmatism-related uplift in central Italy', *Scientific Reports*, vol. 7, no. 1, p. 2517, 2017.
[26] F. Marra *et al.*, 'Volcano-tectonic deformation in the Monti Sabatini Volcanic District at the gates of Rome (central Italy): evidence from new geochronologic constraints on the Tiber River MIS 5 terraces', *Scientific Reports*, vol. 9, no. 1, p. 11496, 2019.
[27] G. Giordano and R. Mazza, 'The Geology of Rome and urban areas: the legacy of Prof. Renato Funiciello', *The geology of Italy*, 2010.
[28] S. Nisio *et al.*, 'Carta delle Cavità sotterranee di Roma', *Pubblicazione ISPRA: Rome, Italy*, 2017.
[29] R. Barzaghi, A. Borghi, D. Carrion, and G. Sona, 'Refining the estimate of the Italian quasi-geoid.', *Bollettino di Geodesia e Scienze affini*, vol. 3, pp. 145–160, 2007.
[30] T. K. Ambrose and M. P. Searle, '3-D structure of the northern Oman-UAE ophiolite: Widespread, short-lived, suprasubduction zone magmatism', *Tectonics*, vol. 38, no. 1, pp. 233–252, 2019.
[31] K. M. Goodenough, M. T. Styles, R. J. Thomas, D. Schofield, R. M. Lilly, and J. McKervey, 'Assembly of the Oman-UAE ophiolite: evidence for a multi-phase magmatic history', 2009.
[32] M. P. Searle, A. G. Cherry, M. Y. Ali, and D. J. Cooper, 'Tectonics of the Musandam Peninsula and northern Oman Mountains: From ophiolite obduction to continental collision', *GeoArabia*, vol. 19, no. 2, pp. 135–174, 2014.
[33] CGT, 'Analisi dei processi di sprofondamento avvenuti in località Valle dei Molini e sviluppo delle potenzialità idriche dell'area (Comuni di Rio Marina e Rio nell'Elba, Isola d'Elba) - Relazione interna del CGT Centro di geotecnologie dell'Università degli Studi di Siena per ASA Azienda Servizi Ambientali S.p.A.' 2015.
[34] G. M. Luberti, A. Prestininzi, and C. Esposito, 'Development of a geological model useful for the study of the natural hazards in urban environments: An example from the eastern sector of Rome (Italy)', *Italian Journal of Engineering Geology and Environment*, vol. 2, pp. 41–62, 2015.
[35] G. Giordano *et al.*, 'The Colli Albani mafic caldera (Roma, Italy): stratigraphy, structure and petrology', *Journal of Volcanology and Geothermal Research*, vol. 155, no. 1–2, pp. 49–80, 2006.
[36] W. M. Telford, L. P. Geldart, and R. E. Sheriff, *Applied geophysics*. Cambridge university press, 1990.
[37] D. Belega and D. Petri, 'Accuracy analysis of the sine-wave parameters estimation by means of the windowed three-parameter sine-fit algorithm', *Digital Signal Processing*, vol. 50, pp. 12–23, 2016.
[38] D. L. Carní and G. Fedele, 'Multi-Sine Fitting Algorithm enhancement for sinusoidal signal characterization', *Computer Standards & Interfaces*, vol. 34, no. 6, pp. 535–540, 2012.
[39] S. J. Wright, 'Coordinate descent algorithms', *Mathematical programming*, vol. 151, no. 1, pp. 3–34, 2015.

[40] A. Wald, ‘Tests of statistical hypotheses concerning several parameters when the number of observations is large’, *Transactions of the American Mathematical society*, vol. 54, no. 3, pp. 426–482, 1943.
[41] D. Freedman and P. Diaconis, ‘On the histogram as a density estimator: L 2 theory’, *Zeitschrift für Wahrscheinlichkeitstheorie und verwandte Gebiete*, vol. 57, no. 4, pp. 453–476, 1981.
[42] G. Phelps, C. Cronkite-Ratcliff, and K. Blake, ‘A time-lapse gravity survey of the Coso geothermal field, China Lake Naval Air Weapons Station, California’, US Geological Survey, 2018.
[43] E. J. Wahyudi and Setianingsih, ‘Repeat gravity observation using CG5 relative gravimeter since 2014 measurements of A10 absolute gravimeter in Bandung and Blora, Indonesia’, in *IOP Conference Series: Earth and Environmental Science*, IOP Publishing, 2025, p. 012017.
[44] Y. Tamura, ‘A harmonic development of the tide-generating potential’, *Bull d’Information Marees Terrestres*, vol. 99, pp. 6813–6855, 1987.
[45] T. F. Baker and M. S. Bos, ‘Validating Earth and ocean tide models using tidal gravity measurements’, *Geophysical Journal International*, vol. 152, no. 2, pp. 468–485, 2003.
[46] M. Rajner, ‘Ocean tidal loading from the gravity measurements at Jozefoslaw observatory’, *Artificial satellites*, vol. 45, no. 4, p. 175, 2010.
[47] H.-G. Wenzel, ‘The nanogal software: Earth tide data processing package ETERNA 3.30’, *Bull. Inf. Marées Terrestres*, vol. 124, pp. 9425–9439, 1996.
[48] A.-K. Cooke, C. Champollion, and N. Le Moigne, ‘First evaluation of an absolute quantum gravimeter (AQG# B01) for future field experiments’, *Geoscientific Instrumentation, Methods and Data Systems*, vol. 10, no. 1, pp. 65–79, 2021.
[49] U. Riccardi, S. Rosat, and J. Hinderer, ‘On the accuracy of the calibration of superconducting gravimeters using absolute and spring sensors: a critical comparison’, *Pure and Applied Geophysics*, vol. 169, no. 8, pp. 1343–1356, 2012.
[50] P. Styles, S. Toon, E. Thomas, and M. Skittrall, ‘Microgravity as a tool for the detection, characterization and prediction of geohazard posed by abandoned mining cavities’, *first break*, vol. 24, no. 5, 2006.
[51] V. Pazzi *et al.*, ‘Integrated geophysical survey in a sinkhole-prone area: Microgravity, electrical resistivity tomographies, and seismic noise measurements to delimit its extension’, *Engineering Geology*, vol. 243, pp. 282–293, 2018.
[52] D. K. Butler, ‘Cavity Detection and Delineation Research. Report 1. Microgravimetric and Magnetic Surveys: Medford Cave Site, Florida.’, 1983.
[53] A. Abdelmaksoud and M. Y. Ali, ‘Petroleum system analysis of Fujairah basin, eastern offshore of the United Arab Emirates’, *Marine and Petroleum Geology*, vol. 170, p. 107157, 2024.
[54] S. Okubo, ‘Advances in gravity analyses for studying volcanoes and earthquakes’, *Proceedings of the Japan Academy, Series B*, vol. 96, no. 2, pp. 50–69, 2020.
[55] S. Rosat and J. Hinderer, ‘Limits of detection of gravimetric signals on Earth’, *Scientific reports*, vol. 8, no. 1, p. 15324, 2018.
[56] M. Sugihara, ‘Gravity monitoring with a CG5 Scintrex autogravimeter’, *ASEG Extended Abstracts*, vol. 2004, no. 1, pp. 1–4, 2004.
[57] T. Jacob, P. Pannet, F. Beaubois, J.-M. Baltassat, and Y. Hannion, ‘Cavity detection using microgravity in a highly urbanized setting: A case study from Reims, France’, *Journal of Applied Geophysics*, vol. 179, p. 104113, 2020.